

Tracing the origin of ore-forming fluids in the Piaotang tungsten deposit, South China: Constraints from in-situ analyses of wolframite and individual fluid inclusion



Jie-Hua Yang^{a,*}, Li-Fang Kang^{a,b}, Liang Liu^{a,*}, Jian-Tang Peng^a, You-Qiang Qi^a

^a State Key Laboratory of Ore Deposit Geochemistry, Institute of Geochemistry, Chinese Academy of Sciences, Guiyang 550081, China

^b University of Chinese Academy of Sciences, Beijing 100049, China

ARTICLE INFO

Keywords:

Fluid inclusion

Source

Wolframite

Piaotang tungsten deposit

South China

ABSTRACT

The Piaotang vein-type tungsten deposit, hosted by Cambrian metasedimentary rocks, is one of the largest vein-type hydrothermal deposits in South China. Wolframite is the dominant ore mineral and intergrown with quartz and cassiterite in the main mineralization stage. Wolframite, cassiterite and quartz crystals have $\delta^{18}\text{O}$ values ranging from 2.5 to 6.8‰, 6.1 to 7.2‰, 10.3 to 13.7‰, respectively. δD values of fluid inclusions in these minerals are very homogenous and lie mostly between -66.1 and -78.3‰. Chondrite-normalized REE patterns of wolframite show HREE enrichment with significant negative Eu anomalies, which are different from those of hosting metasedimentary rocks. H-O isotopes of fluid inclusions and trace elements of wolframite indicated that the ore-forming fluids in the Piaotang tungsten deposit are dominantly magmatic in origin. Metamorphic and meteoric fluids were not involved in the main mineralized stage although the wolframite-quartz veins were hosted by metasedimentary rocks. Element pairs Zr/Hf and Y/Ho of wolframite are remarkably fractionated ($\text{Zr}/\text{Hf} = 13.4\text{--}34.6$, $\text{Y}/\text{Ho} = 10.0\text{--}14.4$). Almost all the analyses of wolframite display unusual tetrad effect REE patterns ($TE_{1-3} > 1.1$). These peculiar trace element characteristics of wolframites indicate that ore-forming fluids have high ligands F and/or Cl contents. LA-ICP-MS analyses of individual fluid inclusion show that ore-forming fluids contain all elements necessary for the formation of wolframite (W, Fe, Mn) and incompatible elements (e.g., Li, Rb, Cs). Cs/Na ratios are positively correlated with Rb/Na ratios. We conclude that the ore-forming fluids were reduced in nature and likely exsolved from the highly evolved granite that concealed in the vicinity of the deposit. Wolframite precipitation resulted from decreasing temperature and pressure of magmatic fluids during infilling along fracture, rather than fluid mixing and fluid-rock interaction.

1. Introduction

Wolframite-bearing quartz vein systems represent a major class of hydrothermal tungsten deposits (Harlaux et al., 2018) and contribute about half of the global W production (Korges et al., 2018). Most of quartz-wolframite vein-type deposits are located within Phanerozoic orogenic belts formed during continental collision- to subduction-related settings (Romer and Kroner, 2016). The most important W resources are found in the South China and the Southeast Asian belt (Fig. 1). The central Andean belt, the East Australian belt, the Karagwe-Ankole belt and the European Variscan belt are also contributed significant tungsten resources (Dewaele et al., 2016; Hulsbosch et al., 2016; Harlaux et al., 2018).

These veins are generally developed either within the granitic body ("endogranitic") or hosted in the enclosing country rocks

("exogranitic"), which are often represented by clastic metasedimentary rocks (Wood and Samson, 2000). However, the genetic link between granite and the formation of wolframite-bearing quartz vein systems remains currently debated, especially metasedimentary rocks hosted wolframite-bearing quartz vein-type tungsten deposit. Constraining the nature and origin of ore-forming fluids are proposed. Most models involve (1) metal-rich magmatic fluids exsolved from granitic magmas (Audáñ et al., 2000; Harlaux et al., 2018; Korges et al., 2018), (2) "external fluids" (metamorphic or meteoric) that circulate around cooling peraluminous granite and leach metals from the peraluminous granite or the country rocks (e.g., Wilkinson, 1990; Zhao and Jiang, 2004), or (3) Mixing of the two (Wei et al., 2012a; Lecumberri-Sánchez et al., 2017; Van Daele et al., 2018).

South China is well known for hosting abundant tungsten resources in the world, which are mostly concentrated in the Nanling

* Corresponding authors.

E-mail addresses: yangjehua@vip.gyig.ac.cn (J.-H. Yang), liuliang@vip.gyig.ac.cn (L. Liu).

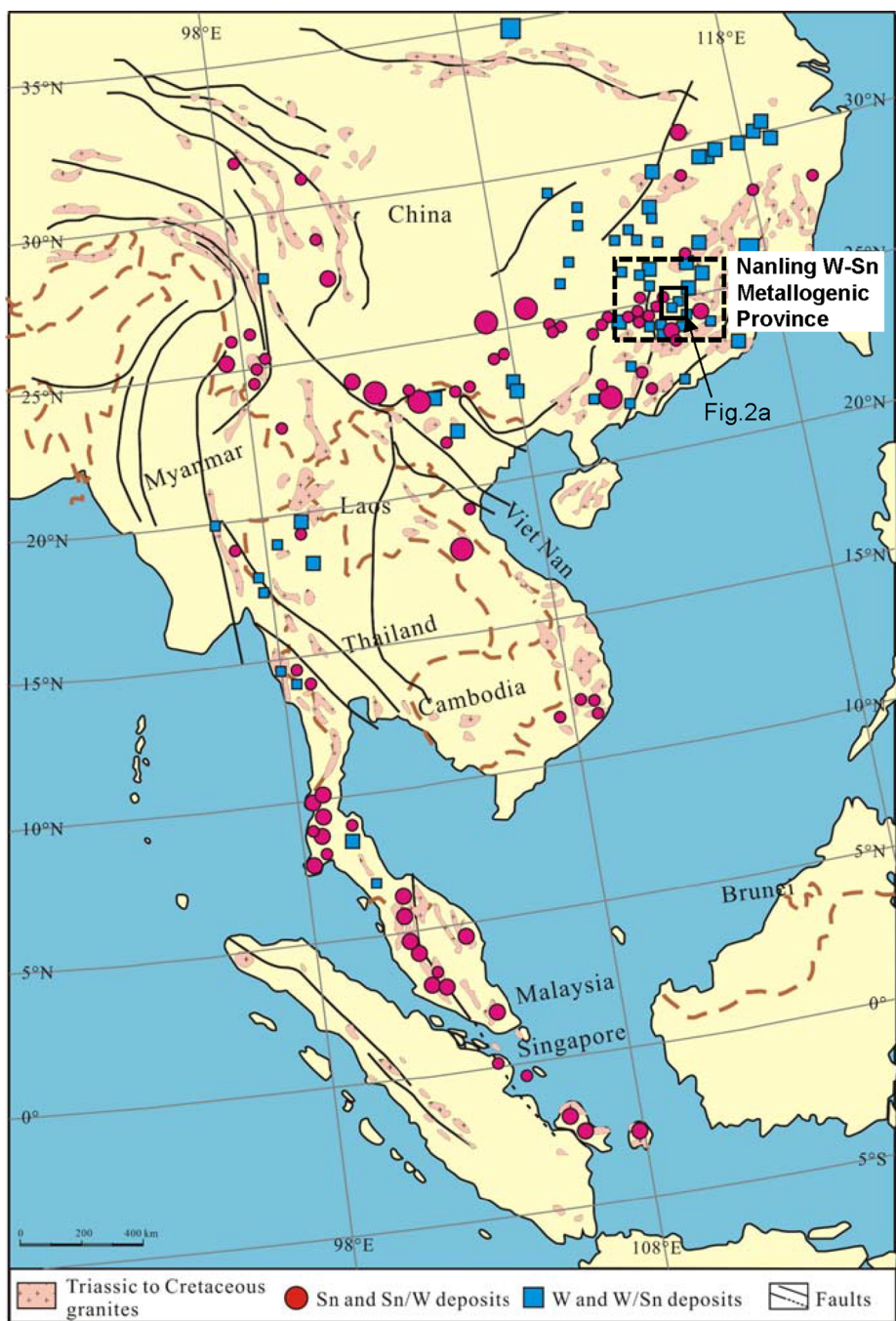


Fig. 1. The most important W-Sn deposits are distributed in the South China and the Southeast Asian belt. Wolframite-bearing quartz vein type tungsten deposit are concentrated in the Nanling W-Sn metallogenic province, South China. Data for W-Sn deposit from previous literatures (Shen et al., 2015; Romer and Kroner, 2016; Zhao et al., 2017).

metallogenic province as wolframite-bearing, quartz vein-type tungsten deposit (Shen et al., 2015; Zhao et al., 2017). Several fluid inclusions (FIs) studies have been carried out in these W deposits, involving microthermometry, Raman spectroscopy, stable isotope (C, H, O, S) analyses and noble gas isotope (He, Ar) analyses (Hu et al., 2012; Wei et al., 2012a,b, 2019; Ni et al., 2015). All of these studies suggest the mixing between a moderate-salinity magmatic fluid exsolved from granitic magma (300–500 °C; 5–15 wt% eq. NaCl) and low-salinity meteoric fluid (100–250 °C; 0–5 wt% eq. NaCl) as being responsible for ore mineral precipitation. Recently, Legros et al. (2018b) suggest that the three or four types aqueous fluid end-members mixed episodically in the mineralization process. Therefore, the source of ore-forming fluid

and the mechanism of ore minerals precipitation remain contentious.

We propose an alternative approach by focusing on the minor and trace element compositions of wolframite and individual fluid inclusions compositions, which are the most likely to record the geochemical compositions of the ore-forming fluids. The present study focused on the Piaotang tungsten deposit which is one of the largest tungsten deposits in the Nanling W-Sn metallogenic province, South China. Individual fluid inclusions compositions, H-O isotopes of ore-forming fluid, and in-situ LA-ICP-MS analyses of wolframite trace elements were obtained to constrain the source of the ore-forming fluids and to clarify the mechanisms of ore mineral precipitation.

2. Geological setting

2.1. Regional geology

The Nanling W-Sn metallogenic province in the South China covers a surface area of about 170,000 km² in Hunan, Jiangxi, Guangdong, and Guangxi provinces (Fig. 1) (Yuan et al., 2018). The basement in this region is mainly composed of weakly metamorphosed Precambrian folded strata, which are unconformably overlain by the folded Paleozoic and Lower Mesozoic strata of shallow marine origin (Yan et al., 2003). Jurassic to Cretaceous granitoids are widespread and some of them host important metallic ore deposits (Hsieh et al., 2008). Various types of tungsten mineralization (i.e., greisen-, skarn-, altered granite- and quartz vein-type) are spatiotemporally and genetically related to the widespread Late Jurassic granitoids (Hu and Zhou, 2012; Mao et al., 2013; Hu et al., 2017), making the Nanling W-Sn metallogenic province as the most important production for tungsten in the world (Ni et al., 2015). Among them, the wolframite-bearing quartz vein type tungsten deposit is the most important in the region and occurred concentratedly between 160 and 150 Ma (Hu and Zhou, 2012; Mao et al., 2013; Yang et al., 2017, 2018).

2.2. Deposit geology

The Piaotang tungsten deposit, located near the Xihuashan deposit (Fig. 2a), is one of the largest tungsten deposits in the Nanling W-Sn metallogenic province and produces 1.5 kt WO₃ per year, ranking

eight largest of China's reserves with 47 kt WO₃ (Legros et al., 2018b). The mineralized quartz veins are hosted by Cambrian metasedimentary rocks that overlain the concealed granite (Fig. 2c and d). The exposed Cambrian metasedimentary rocks of the mining areas consist mainly of sandstone and slate, with minor siliceous slate (Ni et al., 2015). Two sets of faults can be observed in the field: E-W-oriented faults intersecting NE-SW-oriented faults (Fig. 2c). The concealed granite was discovered by drill hole during exploration and emplaced during the Jurassic with zircon U-Pb age of 159.8 ± 1.5 Ma (Zhang et al., 2017). The age of W mineralization was determined to be 159.5 ± 1.5 Ma based on cassiterite U-Pb dating (Zhang et al., 2017).

The Piaotang tungsten deposit is a typical wolframite-bearing quartz vein-type deposit. Ore veins trend EW and dip steeply to the north or nearly vertical in mining area (Fig. 2c and d). The thickness of this vein decreases from the top to the bottom, from a few centimeters to more than one meter (Fig. 2d). Based on mineral assemblages, crosscutting relationships and textures, the framework of three principal paragenetic stages can be identified: an early silicate-oxide stage (stage I) followed by a sulfide stage (stage II) and finally by carbonate stage (stage III).

The stage I is the main stage of tungsten mineralization and consists mainly of massive quartz with wolframite, cassiterite, molybdenite, beryl, feldspar. Wolframite, as the most abundant ore mineral, occurs mainly as euhedral, dark-brown masses. Euhedral wolframite is mainly found attached to the vein walls, with a central filling of massive quartz (Fig. 3a and d). Locally, the wolframite-quartz vein also contains minor cassiterite, feldspar, molybdenite, chalcopyrite, arsenopyrite, or pyrite (Fig. 3b and c). Molybdenite, the earliest sulfide, occurs as euhedral or

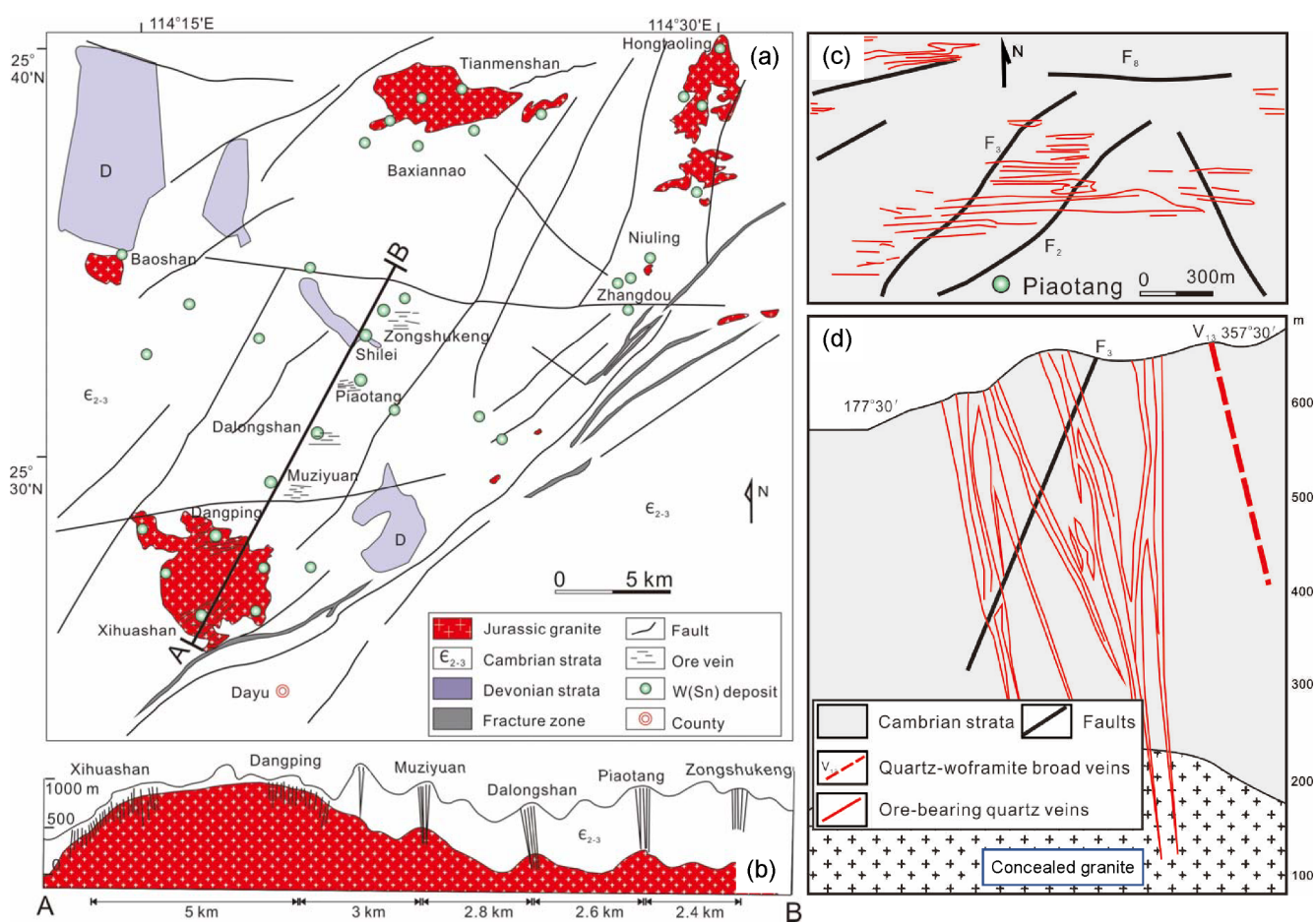


Fig. 2. Geological map of tungsten cluster of Xihuashan-Dangping-Muziyuan-Dalongshan-Piaotang-zongshukeng in the Nanling W-Sn metallogenic province (a), Cross section along Xihuashan-Dangping-Muziyuan-Dalongshan-Piaotang-zongshukeng (b), geological map of the Piaotang tungsten deposit, and Cross section along the No. 12 exploration line in the Piaotang deposit (d). (a) and (b) are modified from Yang et al. (1981). (c) and (d) are modified from Zhang et al. (2017).

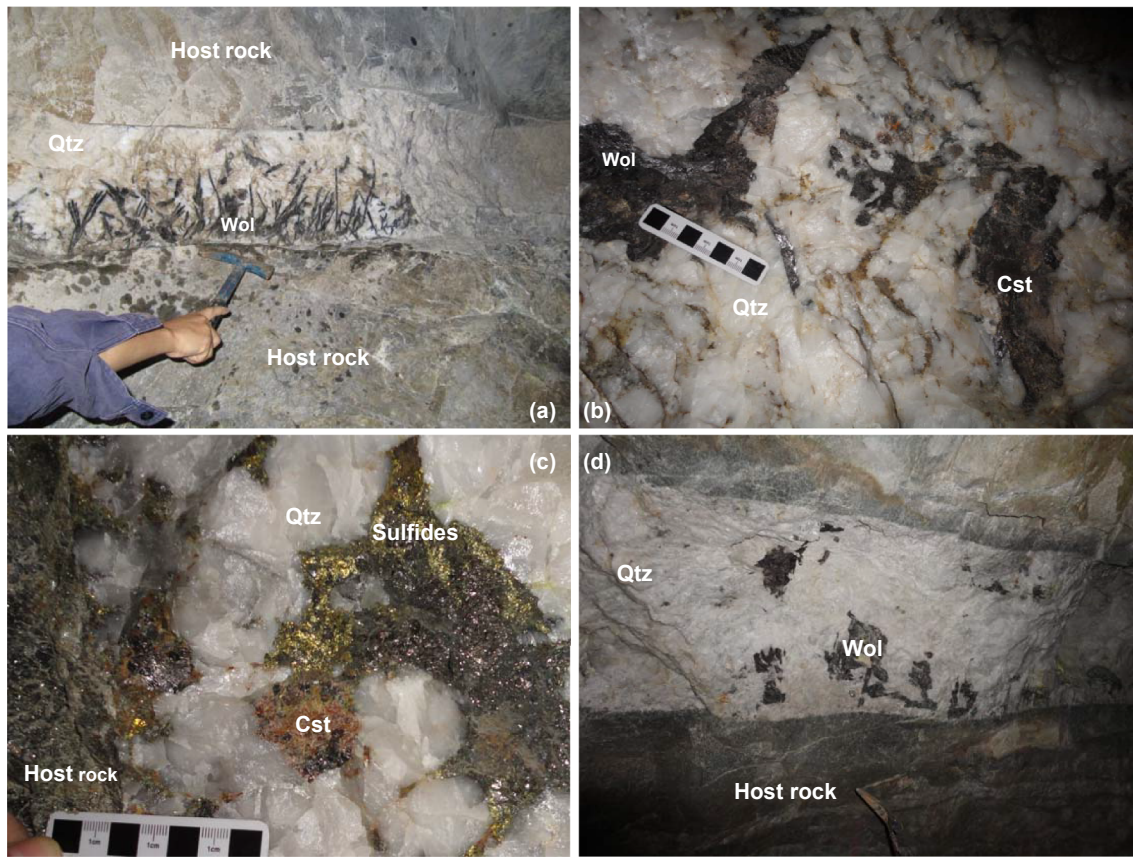


Fig. 3. Photographs of ore and gangue minerals in vein system. Wol: wolframite, Qtz: quartz, Cst: cassiterite.

anhedral masses at vein margins or intergrown with chalcopyrite near vein centers, and arsenopyrite occurs as euhedral or anhedral masses that is intergrown with wolframite.

The sulfide stage (stage II) is characterized the presence of pyrite, arsenopyrite, chalcopyrite, sphalerite, galena, and sphalerite, with trace amounts of wolframite and cassiterite (Fig. 3c). The sulfides clearly postdated wolframite precipitation, and are characterized by a great mineralogical diversity (Fig. 4). The dominant sulfide mineral is pyrite which is associated with subordinate amounts of arsenopyrite, pyrite, sphalerite and chalcopyrite (Fig. 4). The main gangue minerals are quartz and fluorite. The minerals that formed during the sulfide stage occur either in distinct quartz-sulfide veins or as a late filling of stage I quartz-wolframite veins. The structural orientation of the vein formed during the sulfide stage is the same as that of stage I veins.

The last stage of carbonate stage (stage III) is represented by numerous barren quartz and calcite veins with trace amounts of chalcopyrite and pyrite but no wolframite. These veins crosscut all other types of veins, locally producing dense stockworks, and are commonly quite thick.

3. Analytical methods

3.1. EPMA and LA-ICP-MS analyses of wolframite

Major element composition of wolframite was determined using a 1720H EPMA equipped with WDS spectrometers at Central South University in Changsha City. An acceleration voltage of 20 kV and a beam current of 20 nA with counting times of 10 s on element peak and 5 s on background position were used. Analytical error was < 1% for

the measured elements. Chemical compositions are expressed in weight percent (%) oxides.

In situ LA-ICP-MS trace element analyses of wolframites were obtained using an Agilent 7700x ICP-MS coupled with a GeoLasPro 193 nm ArF excimer laser ablation system) at Institute of Geochemistry, Chinese Academy of Sciences (IGCAS). Analyses were done on homogeneous zone within the wolframite samples, which were identified after EPMA analyses and are devoid of micro-cracks, micro-inclusions, or alteration features. Laser ablation was performed with a constant 5 Hz pulse frequency and a constant fluence of 4.5 J/cm² by focusing the beam at the sample surface. Helium was used as carrier gas to transport the laser-generated particles from the ablation cell to the ICP-MS and argon was added as an auxiliary gas via a flow adapter before the ICP torch. The reference materials NIST SRM 610 and 612 were used as external standards for calibration of all analyses. The NIST SRM 610 was used as primary reference material for the quantification, whereas the NIST SRM 612 was used as secondary control standards to test the accuracy and precision. For all analyses of wolframite, W was used as internal standard determined from the EPMA analyses. Off-line data was processed using the ICPDatacal 11.5 (Liu et al., 2010).

3.2. LA-ICP-MS analysis of individual fluid inclusions

The chemical compositions of individual fluid inclusion were analyzed by LA-ICP-MS at IGCAS by using Agilent 7900 ICP-MS equipped with a GeoLasPro 193 nm ArF excimer laser. Laser repetition of 10 Hz and energy density of 10 J/cm² were used during the analyses. Laser spot size was adjusted from 16 to 44 μm for the fluid inclusion analyses. The raw LA-ICP-MS data were reduced using the SILLS software

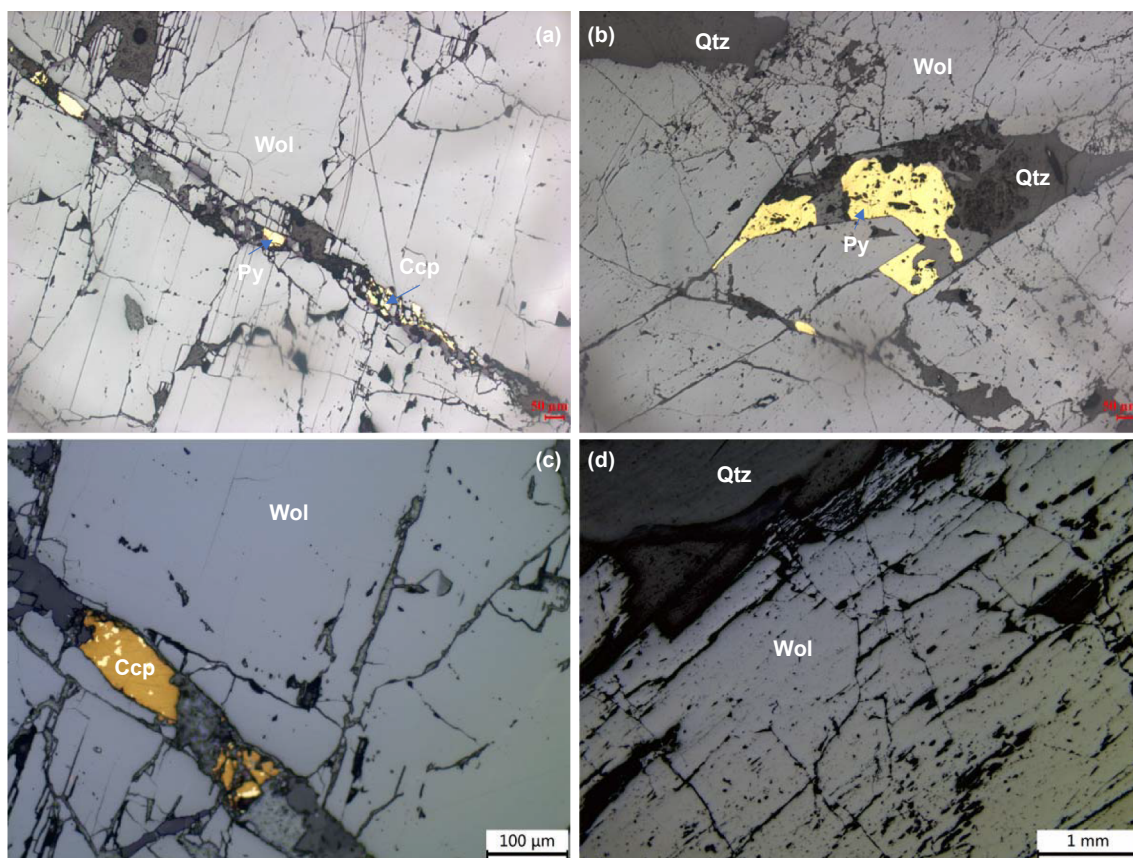


Fig. 4. Photomicrographs showing the typical composition and texture of ores in the Piaotang deposit. Wol: wolframite, Qtz: quartz, Cst: cassiterite, Py: pyrite, Ccp: Chalcopyrite.

(Guillong et al., 2008). NIST SRM 610 was used as external standard and analyzed twice every 10 analyses. The about average of NaCl equivalent 5.0 wt% concentrations in the fluid inclusion trapped in quartz, which were obtained by Ni et al. (2015). The charge-balance method was adopted to correct the modeled amounts of Na (5.0 wt% eq NaCl) for salinity contributions of other chloride salts (Allan et al., 2005). The detail analytical process is described by Lan et al. (2018).

3.3. Hydrogen and oxygen isotopes analysis

We performed a comprehensive stable isotope study on the main ore and gangue minerals. Representative samples from the principal mineralization stage (stage I) of the Piaotang deposit were chosen for picking mineral separates for stable isotope analyses. Most of quartz, cassiterite and wolframite crystals for stable isotope analyses were picked from the same samples. Hydrogen (H) and Oxygen (O) isotopes analysis of quartz, cassiterite and wolframite was carried out by using a Finnigan MAT-253 mass spectrometer at the Analytical Laboratory of the Beijing Research Institute of Uranium Geology, China. Water was released from quartz, cassiterite and wolframite by heating to ca. 600 °C in an induction furnace and then reacted with heated zinc powder at 400 °C to produce H₂ for hydrogen isotopic analysis. Quartz, cassiterite and wolframite grains were ground to powder and then reacted with BrF₅ at 500–600 °C for 14 h to generate O₂. With the catalysis of platinum, the O₂ reacted with graphite at 700 °C to produce CO₂ for oxygen isotopic analysis. The analytical results of ²H/¹H and ¹⁸O/¹⁶O ratios are expressed as the conventional δD and δ¹⁸O values in per mil (‰) relative to the Vienna Standard Mean Ocean Water (VSMOW) with

precisions of 1‰ and 0.2‰, respectively.

The δ¹⁸O_{V-SMOW} for water equilibrated with quartz were calculated using the equation from Matsuhisa et al. (1979) based on δ¹⁸O_{V-SMOW} value of quartz and equilibrium temperature. The δ¹⁸O_{V-SMOW} for water equilibrated with wolframite and cassiterite using the equation from Zhang et al. (1994) according to δ¹⁸O_{V-SMOW} value of wolframite and cassiterite. Oxygen isotopic exchange equilibrium temperatures for texturally coexisting mineral pairs (quartz-wolframite and quartz-cassiterite) was calculated using experimentally determined calibrations method of Zhang et al. (1994).

3.4. Major and trace elements analyses

Major elements of concealed granite and metasedimentary rock were analyzed using a RANalytical Axios-advance (Axios PW4400) X-ray fluorescence spectrometer at IG-CAS on fused glass beads. Trace elements were analyzed using a Perkin-Elmer Sciex ELAN 6000 inductively coupled plasma mass spectrometer (ICP-MS) at IGCAS. Analytical procedures are similar to those described by Qi et al. (2000).

4. Results

4.1. Fluid inclusion petrography

The studied samples contain abundant fluid inclusions (FIs), ranging in diameter between 6 and 25 μm, many of which are rounded rectangles and ellipsoids. Representative fluid inclusion assemblages are shown in Fig. 5. The vast majority of the inclusions are liquid-rich two

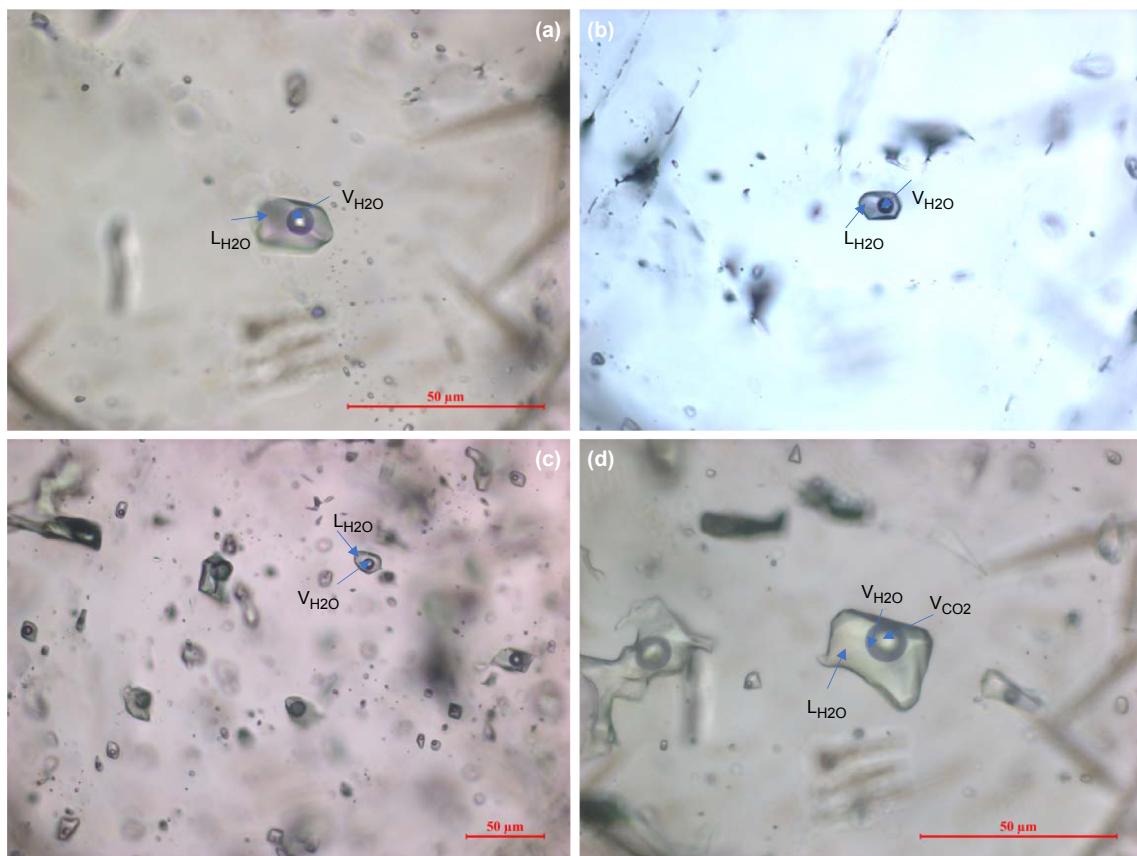


Fig. 5. Photomicrographs of representative fluid inclusion types in quartz.

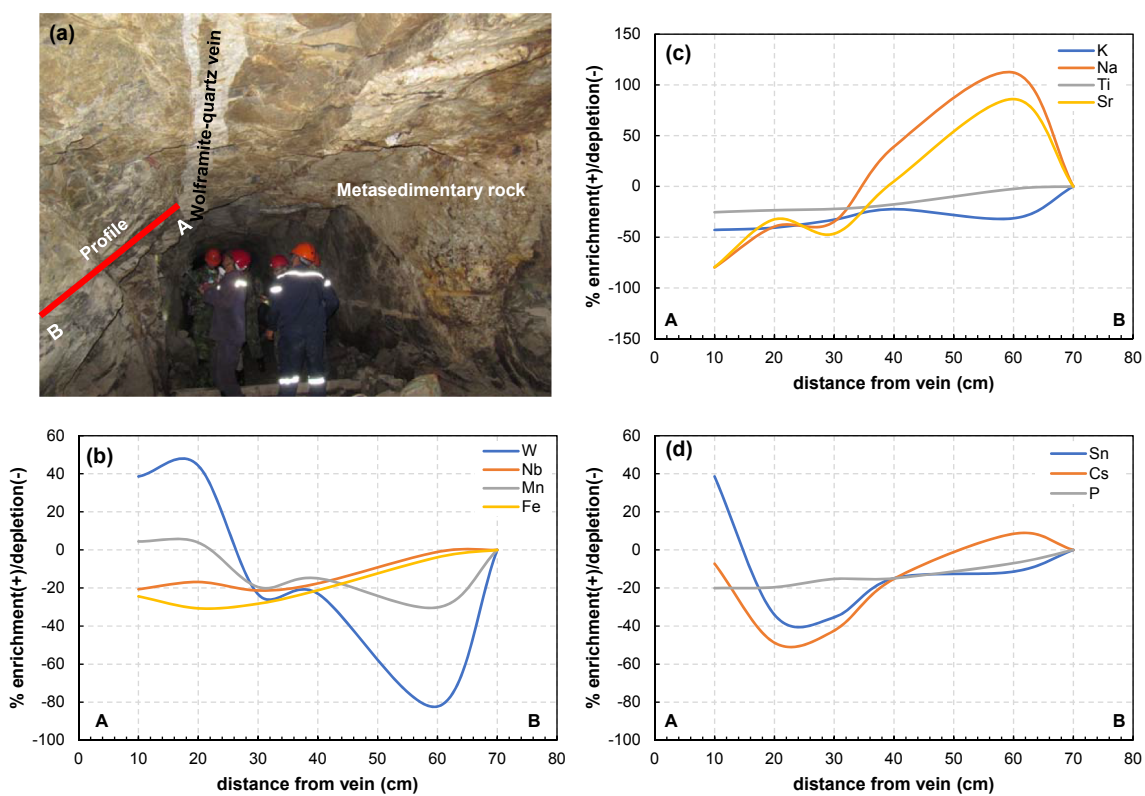


Fig. 6. The variation of chemical composition of hosting rock as function of distance from vein along profile A-B.

Table 1
Chemical compositions of individual fluid inclusion trapped by quartz.

Spot	Li7 ppm	Na23 ppm	Mg24 ppm	Al27 ppm	K39 ppm	Sc45 ppm	Ti49 ppm	Mn55 ppm	Fe57 ppm	Cu63 ppm	Zn66 ppm
1	3993	14,949	< LOD	12,517	< LOD	450.3	< LOD	< LOD	< LOD	1192	< LOD
2	376	14,949	< LOD	< LOD	< LOD	48.0	< LOD	< LOD	< LOD	138	< LOD
3	3330	14,949	< LOD	3635	< LOD	< LOD	< LOD	< LOD	< LOD	1721.5	< LOD
4	< LOD	11,022	1243	839	2678	< LOD	< LOD	25,438	122,424	< LOD	1891.0
5	9194	14,949	< LOD	< LOD	< LOD	< LOD	22/8.4	< LOD	< LOD	3344	< LOD
6	16,045	14,949	< LOD	< LOD	< LOD	< LOD	2640.4	< LOD	< LOD	7541	< LOD
7	2836	1562	< LOD	< LOD	22,768	540.0	< LOD	< LOD	< LOD	1,425	< LOD
8	< LOD	13,958	52.1	< LOD	1518	3.3	79.2	< LOD	< LOD	6.9	6.7
9	9	< LOD	6624	4400	6775	< LOD	< LOD	4416	62,549	< LOD	4113.3
10	2001	1260	< LOD	< LOD	23,282	293.2	< LOD	< LOD	< LOD	933	< LOD
11	< LOD	13,482	< LOD	9239	2489	< LOD	67.9	< LOD	< LOD	< LOD	< LOD
12	< LOD	12,184	1461	2616	< LOD	< LOD	51.80	13,791	114,088	< LOD	2207.5
13	< LOD	10,423	2392	2757	< LOD	< LOD	5025	25,452	167,508	< LOD	2446.9
14	< LOD	14,519	227	545	< LOD	< LOD	218	1889	12,639	< LOD	267.3
15	< LOD	11,540	1802	4107	< LOD	< LOD	1036	15,814	111,855	< LOD	1745.0
16	< LOD	13,938	534	3001	< LOD	< LOD	752	6487	55,285	< LOD	536.6
17	< LOD	14,644	161	262	< LOD	< LOD	145.5	1113	10,948	< LOD	224.1
18	1293	165	< LOD	25,143	202.4	< LOD	< LOD	< LOD	< LOD	751	< LOD
19	1117	1599	< LOD	< LOD	61.3	< LOD	< LOD	< LOD	< LOD	587	< LOD
20	18.5	14,807	< LOD	< LOD	22/70.4	< LOD					
21	< LOD	14,635	166	346	< LOD	< LOD	124	< LOD	< LOD	7532	< LOD
22	< LOD	13,806	604	2284	< LOD	< LOD	1451	3266	51,812	< LOD	648.8
23	860	1018	< LOD	< LOD	23,693	< LOD	365.9	< LOD	< LOD	318	< LOD
24	46	14,821	68	565	< LOD	< LOD	97	440	52.62	570	193.0
25	< LOD	14,563	204	759	< LOD	< LOD	245	1966	20,716	445.1	8353.6
26	< LOD	9271	3001	65,464	< LOD	< LOD	1933	27,924	350,907	1239	3354.3
27	< LOD	11,113	2028	37,733	< LOD	< LOD	773	13,571	100,896	< LOD	180
28	264	13,874	568	10,716	< LOD	< LOD	694	1141	35,392	727.5	482.5
29	< LOD	13,654	684	2241	< LOD	< LOD	367	< LOD	38,892	< LOD	126.0
30	< LOD	14,749	106	842	< LOD	< LOD	78	461	5749	< LOD	261.42
31	< LOD	13,276	884	6208	< LOD	< LOD	379	10,145	80,641	< LOD	529.1
32	< LOD	14,493	241	2933	< LOD	< LOD	434	1260	21,320	< LOD	27.5
33	104	13,995	< LOD	< LOD	1620	< LOD	23	< LOD	< LOD	28,577	286.3
34	< LOD	13,867	572	567	< LOD	< LOD	472	< LOD	< LOD	< LOD	< LOD
35	104	13,134	< LOD	1336	< LOD	< LOD	3086	< LOD	< LOD	< LOD	< LOD
36	333	14,520	< LOD	1310	730	< LOD	< LOD	3482	1211	137,400	< LOD
37	< LOD	11,808	1660	18,675	< LOD	< LOD	< LOD	1559	1685	82,544	< LOD
38	< LOD	12,308	1396	4372	< LOD	< LOD	< LOD	1176	6415	46,168	643.8
39	< LOD	13,171	940	8012	< LOD	< LOD	1275	< LOD	< LOD	< LOD	< LOD
40	464	13,716	255	1713	< LOD	< LOD	116.5	116.5	433.7	6228	98.3
41	169	14,719	122	563	< LOD	< LOD	1051	54.9	8753	< LOD	122.0
42	< LOD	14,725	118	341	< LOD	< LOD	24.9	< LOD	7753	30,921	2560
43	100	14,854	43	49	< LOD	< LOD	79.8	175	< LOD	39.5	< LOD
44	85	14,882	35	909	< LOD	< LOD	37.6	302	2089	< LOD	50.0
45	< LOD	14,394	11	4414	< LOD	< LOD	13.6	< LOD	< LOD	< LOD	< LOD
46	< LOD	13,864	574	15,924	< LOD	< LOD	678	6921	40,923	< LOD	530.8
47	< LOD	3763	5911	7753	< LOD	< LOD	151.7	< LOD	4776.3	< LOD	331.9
48	730	357	< LOD	24,818	< LOD	< LOD	1458	< LOD	45,319	< LOD	390.3
49	< LOD	13,005	1027	2044	< LOD	< LOD	218	198	4870	< LOD	92.3
50	< LOD	14,775	92	160	< LOD	< LOD	49.7	773	1580	< LOD	624.9
51	< LOD	14,299	344	4406	< LOD	< LOD	170	121	5348	< LOD	148.8
52	< LOD	14,752	104	14,107	< LOD	< LOD	28	84	794	< LOD	88.0
53	157	14,107	14	1388	< LOD	< LOD	13	13	193.3	< LOD	133.3

(continued on next page)

Table 1 (continued)

Spot	Li7 ppm	Na23 ppm	Mg24 ppm	Al27 ppm	K39 ppm	Sc45 ppm	Ti49 ppm	Mn55 ppm	Fe57 ppm	Cu63 ppm	Zn66 ppm	
54	< LOD	14,490	242	17	< LOD	69	1717	14,400	< LOD	< LOD	225.2	
55	< LOD	9588	2833	42,512	< LOD	8963	5405	321,668	< LOD	< LOD	3625.4	
56	< LOD	12,647	1217	1718	< LOD	614	2217	66,155	< LOD	< LOD	1114.9	
57	< LOD	13,328	856	1099	< LOD	14	3236	45,765	< LOD	< LOD	270.7	
58	< LOD	14,110	443	365	< LOD	219	4642	35,659	< LOD	< LOD	555.7	
59	886	1394	< LOD	< LOD	23,054	240.6	< LOD	< LOD	< LOD	353.4	< LOD	
60	< LOD	13,885	562	1688	< LOD	485	6417	37,322	< LOD	< LOD	842.7	
61	81	14,736	112	335	< LOD	36	1701	7988	< LOD	< LOD	141.4	
62	< LOD	12,207	1449	4867	< LOD	2127	16,550	85,523	< LOD	< LOD	1126.1	
63	662	2745	< LOD	< LOD	20,756	206.1	< LOD	< LOD	< LOD	365.9	< LOD	
64	< LOD	4556	5493	28,747	< LOD	5228	67,756	443,793	< LOD	< LOD	7908.6	
65	< LOD	13,328	857	3728	< LOD	1018	528	50,223	< LOD	< LOD	888.3	
66	226	14,838	58	105	< LOD	92	217	2659	< LOD	< LOD	26.1	
67	< LOD	14,602	184	410	< LOD	368	981	11,642	< LOD	< LOD	169.6	
68	< LOD	7537	3917	31,698	< LOD	3723	28,077	234,034	< LOD	< LOD	2829.8	
69	435	14,610	179	3938	< LOD	52	440	9678	< LOD	< LOD	255.0	
70	469	2764	< LOD	< LOD	20,723	38.3	< LOD	< LOD	< LOD	209	< LOD	
71	687	1797	< LOD	< LOD	22,368	141.3	< LOD	< LOD	< LOD	208	< LOD	
72	< LOD	2151	< LOD	< LOD	21,766	200.0	< LOD	< LOD	< LOD	190	< LOD	
Av.	1623	11,390	1028	6718	12,138	465	1265	8784	76,015	954	1277	
Spot	As75 ppm	Rb85 ppm	Sr88 ppm	Nb93 ppm	Mo95 ppm	Ag107 ppm	Sn118 ppm	Cs133 ppm	Ta181 ppm	W182 ppm	Pb208 ppm	Bi209 ppm
1	< LOD	384.2	3.7	< LOD	< LOD	5317.3	< LOD	< LOD	< LOD	0.8	< LOD	
2	< LOD	66.7	1.1	< LOD	< LOD	636.7	107.2	< LOD	< LOD	0.1	< LOD	
3	< LOD	495.7	6.7	< LOD	< LOD	7115.3	< LOD	< LOD	< LOD	114.1	< LOD	
4	3280.7	< LOD	14.2	< LOD	< LOD	158.6	142.0	0.0	< LOD	35.5	82.4	
5	< LOD	1764.2	< LOD	< LOD	< LOD	< LOD	0.3	2.4	< LOD	< LOD		
6	< LOD	4068.0	< LOD	< LOD	< LOD	41105.5	< LOD	< LOD	< LOD	< LOD	< LOD	
7	< LOD	733.4	< LOD	< LOD	< LOD	8847.0	< LOD	< LOD	< LOD	< LOD	< LOD	
8	177.7	110.3	4.3	0.6	< LOD	< LOD	358.5	0.4	11.5	4.0	< LOD	
9	12715.8	< LOD	55.6	< LOD	< LOD	345.0	< LOD	513.3	< LOD	51.5	178.8	
10	< LOD	336.3	< LOD	< LOD	< LOD	5453.3	< LOD	0.0	< LOD	0.0	< LOD	
11	32.0	3.2	< LOD	< LOD	< LOD	42.4	< LOD	5.4	< LOD	5.4	< LOD	
12	4429.3	0.1	< LOD	< LOD	< LOD	252.7	< LOD	235.7	< LOD	8.2	22.6	
13	6699.5	< LOD	2.3	< LOD	< LOD	168.1	< LOD	281.4	< LOD	7.1	0.1	
14	573.0	< LOD	108.3	< LOD	< LOD	14.8	< LOD	74.7	< LOD	0.1	1.9	
15	3141.7	< LOD	20.3	< LOD	< LOD	91.8	100.4	< LOD	275.0	1.6	31.6	
16	1602.8	12.4	< LOD	< LOD	< LOD	67.7	< LOD	176.6	0.1	32.9	35.2	
17	375.9	6.2	1.6	8.6	22.6	45.4	< LOD	45.4	< LOD	31.8	7.9	
18	< LOD	245.8	< LOD	< LOD	< LOD	4447.4	< LOD	< LOD	< LOD	< LOD	< LOD	
19	< LOD	241.5	< LOD	< LOD	< LOD	4663.5	< LOD	< LOD	< LOD	< LOD	< LOD	
20	29.0	< LOD	1.4	9.7	< LOD	14.0	< LOD	< LOD	170.0	< LOD	< LOD	
21	305.2	50.2	1.4	8.6	22.6	68.8	0.0	0.5	1.5	8.5	42.3	
22	1800.9	< LOD	19.4	< LOD	37.0	105.9	< LOD	181.1	3.0	6.4	< LOD	
23	< LOD	201.8	< LOD	0.0	< LOD	3821.7	< LOD	< LOD	< LOD	< LOD	< LOD	
24	521.7	163.4	1.3	0.0	< LOD	9.5	< LOD	397.8	17.8	22.3	1.8	
25	858.3	29.9	0.6	< LOD	< LOD	14.1	< LOD	267.5	1.2	6.8	38.7	
26	11332.8	881.3	68.8	< LOD	< LOD	500.5	< LOD	877.0	0.3	76.4	333.6	
27	4214.2	< LOD	27.1	< LOD	< LOD	111.8	< LOD	375.1	< LOD	1.8	60.0	
28	1573.7	147.0	1.0	0.2	< LOD	54.2	< LOD	602.0	< LOD	55.0	77.6	
29	1700.4	< LOD	11.3	0.1	< LOD	34.2	< LOD	97.8	0.1	68.0	12.0	

(continued on next page)

Table 1 (continued)

Spot	As75 ppm	Rb85 ppm	Sr88 ppm	Nb93 ppm	Mo95 ppm	Ag07 ppm	Sn118 ppm	Cs133 ppm	Ta181 ppm	W182 ppm	Pb208 ppm	Bi209 ppm
30	192.2	< LOD	7.4	1.2	13.0	4.5	< LOD	54.0	< LOD	21.3	5.1	3.0
31	2892.2	< LOD	< LOD	< LOD	63.7	137.8	< LOD	295.4	< LOD	108.1	3.7	43.3
32	914.3	< LOD	11.7	< LOD	< LOD	4.2	< LOD	137.2	1.6	9.9	< LOD	15.3
33	99.2	56.2	< LOD	169.1	< LOD	0.8	< LOD	< LOD				
34	1521.5	< LOD	0.4	< LOD	< LOD	126.0	< LOD	182.1	6.7	18.8	16.0	28.0
35	166.0	160.4	0.9	< LOD	< LOD	< LOD	< LOD	496.9	< LOD	23.5	< LOD	< LOD
36	149.0	23.9	< LOD	1.9	< LOD	< LOD	< LOD	54.7	< LOD	30.9	< LOD	< LOD
37	4281.4	< LOD	2.1	< LOD	< LOD	92.5	< LOD	271.0	< LOD	136.7	< LOD	36.5
38	3863.7	< LOD	2.1	< LOD	67.8	105.7	< LOD	219.5	< LOD	18.7	0.5	47.1
39	2755.7	< LOD	0.6	< LOD	23.9	< LOD	< LOD	169.7	0.1	19.7	10.5	30.4
40	< LOD	43.7	9.7	< LOD	< LOD	5.1	2.5	11.5	55.9	< LOD	4.5	< LOD
41	234.3	< LOD	27.7	< LOD	< LOD	1.6	< LOD	72.5	< LOD	1.7	< LOD	4.2
42	615.5	164.9	4.8	< LOD	< LOD	8.8	< LOD	423.2	< LOD	24.7	4.1	4.1
43	190.8	68.4	0.9	< LOD	< LOD	0.3	< LOD	238.7	< LOD	0.7	0.5	3.2
44	149.4	64.5	1.5	< LOD	< LOD	3.0	< LOD	248.3	< LOD	1.0	0.4	1.9
45	< LOD	31.8	50.9	< LOD	< LOD	37.9	42.5	< LOD	75.9	< LOD	0.6	< LOD
46	1536.0	< LOD	10.3	< LOD	41.6	41.8	< LOD	658.4	< LOD	205.4	< LOD	18.7
47	10246.7	< LOD	41.6	< LOD	171.5	< LOD	< LOD	2993.4	< LOD	654.8	< LOD	318.7
48	< LOD	< LOD	7.5	< LOD	< LOD	0.1	< LOD	30.4	< LOD	0.0	< LOD	< LOD
49	1984.3	< LOD	123.4	2.6	< LOD	< LOD	< LOD	147.8	3.6	52.7	17.3	40.9
50	887.0	55.4	1.1	< LOD	< LOD	9.7	< LOD	479.9	< LOD	11.1	0.1	11.5
51	2288.8	62.8	1.9	< LOD	< LOD	65.6	< LOD	542.8	< LOD	27.1	22.8	63.6
52	738.4	81.2	1.0	< LOD	1.5	0.0	< LOD	360.8	0.3	10.3	0.9	7.4
53	252.1	478.8	154.8	0.0	< LOD	0.0	< LOD	215.9	0.1	0.9	46.4	1.4
54	8884.7	< LOD	19.4	0.7	< LOD	46.3	113.4	< LOD	106.5	< LOD	0.1	4.6
55	2055.5	< LOD	0.3	< LOD	0.7	0.7	< LOD	739.9	18.5	3.8	89.3	184.4
56	1486.5	< LOD	4.1	< LOD	98.0	0.0	< LOD	174.1	3.8	36.7	64.6	33.1
57	835.9	< LOD	0.6	< LOD	0.6	0.0	< LOD	210.7	0.8	0.3	9.1	9.1
58	1188.7	< LOD	1.9	< LOD	6.3	226.8	358.0	< LOD	106.5	< LOD	0.1	< LOD
59	366.9	27.1	< LOD	< LOD	6.4	46.3	13.4	< LOD	366.1	< LOD	5.3	33.1
60	3168.7	< LOD	99.9	< LOD	27.1	0.7	< LOD	9.7	< LOD	299.8	0.5	3.7
61	63.7	< LOD	0.1	< LOD	0.0	0.0	< LOD	1.8	< LOD	582.8	10.3	59.1
62	641.0	< LOD	5.2	< LOD	5.2	0.0	< LOD	37.9	< LOD	2091.4	< LOD	< LOD
63	9518.2	< LOD	145.8	< LOD	7.9	108.9	< LOD	2216.5	< LOD	0.0	< LOD	< LOD
64	22256.7	< LOD	63.6	< LOD	6.4	50.7	< LOD	1074.4	< LOD	1501.2	18.3	354.0
65	1295.1	< LOD	76.1	< LOD	6.4	142.6	< LOD	90.6	< LOD	174.8	85.0	34.5
66	94.0	< LOD	95.9	< LOD	76.1	0.0	< LOD	3.6	< LOD	63.3	0.1	2.4
67	2146.6	< LOD	94.0	< LOD	72	0.0	< LOD	1.7	< LOD	371.4	16.2	2.2
68	355.7	< LOD	145.8	< LOD	145.8	6.4	< LOD	89.9	< LOD	1245.7	16.0	190.8
69	< LOD	< LOD	76.1	< LOD	< LOD	0.0	< LOD	151.8	< LOD	1791.2	1.8	7.8
70	< LOD	< LOD	95.9	< LOD	< LOD	0.0	< LOD	2146.6	< LOD	0.0	< LOD	< LOD
71	< LOD	< LOD	94.0	< LOD	< LOD	0.0	< LOD	2208.7	< LOD	< LOD	< LOD	< LOD
72	< LOD	0.0	< LOD	0.0	< LOD	0.0	0.000247	4				
Av.	2715	319	22	7	35	108	7090	300	4	32	23	52

LOD: limit of detection.

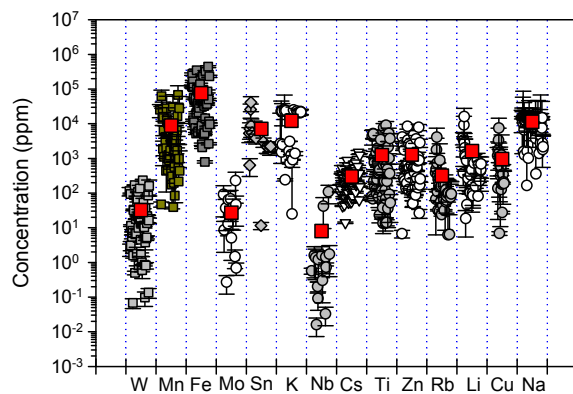


Fig. 7. The element concentrations of the ore-forming fluids in Piaotang tungsten deposit. The red filled boxes denote average values.

phases inclusions. On the basis of Raman spectroscopy analyses, the main component of the volatile phase in FIs is dominated by H_2O with minor CO_2 and CH_4 in some cases. Multiple generation of secondary inclusions are very abundant in most samples and their trails are locally very dense, which appears possible that some of the original primary fluid inclusions subsequently refilled. Some of the secondary inclusions have healed very well with a scattered distribution, which texturally appear isolated and look like primary but are in fact secondary in origin. We have solved these problems by a particularly careful selection of primary and pseudosecondary fluid inclusions, where we adhered strictly to the criteria for these fluid inclusion types established by Roedder (1984) and Goldstein and Reynolds (1994).

4.2. Major and trace elements of granite and host rock

The major and trace elements of concealed granite and host rock are presented in Appendix A. The enrichment and depletion of elements in the host rock have been calculated based on a normalization to Zr and

using the most distal sample from vein as reference approximating the unaltered local host rock. The detail calculated method is similar to Lecumberri-Sanchez et al. (2017). The variation of the chemical composition of the host rock as a function of distance from the vein are illustrated in Fig. 6.

4.3. Chemical compositions of fluid inclusions

Two-phase aqueous primary FIs trapped in quartz associated with the main mineralized stage (stage I) were selected for LA-ICP-MS analyses. A total of 72 fluid inclusions were conducted. Element concentrations in FIs are listed in Table 1 and Fig. 7.

LA-ICP-MS analyses show that all elements necessary for the formation of wolframite (W, Fe, Mn) and cassiterite (Sn) can be detected in FIs (Fig. 7). Fluids are systematically enriched in incompatible elements such as Li, Cs and Rb (Fig. 7). Rb/Na ratios vary with Cs/Na ratio in the FIs. Cs contents is positively correlated with As, W and Ti contents (Fig. 8).

4.4. Major and trace element compositions of wolframite

Chemical compositions of wolframite from the Piaotang deposit determined by EPMA and LA-ICP-MS are given in Tables 2 and 3, respectively. Structural formulae of wolframite were calculated on the basis of 4 atoms of oxygen in number of atoms per formula unit (apfu). The wolframite from the Piaotang deposit are characterized by variable $\text{Fe}/(\text{Fe} + \text{Mn})$ values (Table 2) ranging from 0.19 to 0.50 and falling in the field of wolframite with $\text{Fe}/(\text{Fe} + \text{Mn})$ between 0.2 and 0.8 definition from White (1981).

Wolframite crystals from the Piaotang deposit contain high Nb (1427–5550 ppm), Sc (9.6–202 ppm), Ti (7.9–80 ppm), Sn (26.4–258 ppm), Ta (14–228 ppm), and U (4.2–24.4) contents. All of the wolframite samples have trace element compositions different from that in metasedimentary rocks (Fig. 9a). Their chondrite-normalized REE patterns show steep LREE and relatively flat HREE patterns with significant negative Eu anomalies and display unusual tetrad effect

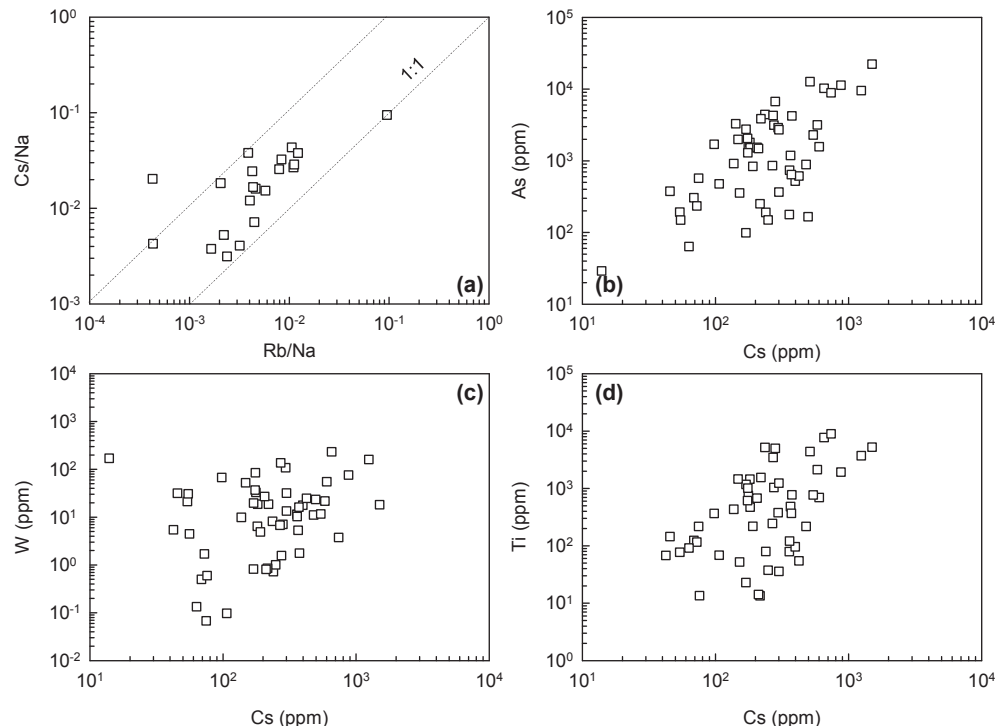


Fig. 8. The variation diagrams of selected element and ratio in fluid inclusion from the Piaotang deposit.

Table 2

Major elements of representative wolframite from the Piaotang tungsten deposit.

Sample/spot	WO ₃ wt%	MnO wt%	Nb ₂ O ₅ wt%	FeO wt%	CaO wt%	Ta ₂ O ₅ wt%	Total wt%	W apfu	Mn apfu	Nb apfu	Fe apfu	Ca apfu	Total apfu	Fe/(Fe + Mn) ratio
PT8A1	76.33	16.97	0.56	6.31	0.030	–	100.2	0.993	0.722	0.013	0.265	0.002	1.99	0.27
PT8B1	75.00	12.24	0.41	11.80	0.012	–	99.5	0.984	0.525	0.009	0.499	0.001	2.02	0.49
PT8C1	76.11	16.30	0.64	7.01	0.008	–	100.1	0.992	0.694	0.014	0.295	0.000	1.99	0.30
PT8D1	74.79	11.92	0.66	11.64	0.039	0.237	99.3	0.984	0.513	0.015	0.494	0.002	2.01	0.49
PT8D2	73.89	12.00	0.58	11.97	0.010	–	98.5	0.978	0.519	0.013	0.512	0.001	2.02	0.50
PT8E1	74.42	15.45	0.48	8.33	0.023	–	98.7	0.983	0.667	0.011	0.355	0.001	2.02	0.35
PT8E2	75.48	15.10	0.43	8.43	0.028	–	99.5	0.990	0.647	0.010	0.357	0.002	2.01	0.36
PT8F1	75.24	12.12	0.32	11.51	0.014	–	99.2	0.990	0.521	0.007	0.489	0.001	2.01	0.48
PT8F2	74.91	19.08	0.61	4.63	0.039	–	99.3	0.983	0.818	0.014	0.196	0.002	2.01	0.19
PT8F3	75.19	17.29	0.63	5.91	0.017	–	99.0	0.989	0.744	0.014	0.251	0.001	2.00	0.25
PT21A1	74.52	15.10	0.16	8.55	0.018	–	98.3	0.989	0.655	0.004	0.366	0.001	2.02	0.36
PT21B1	76.81	15.00	0.21	8.46	0.010	–	100.5	0.998	0.637	0.005	0.355	0.001	2.00	0.36
PT21B2	75.23	15.26	0.14	8.62	0.025	0.285	99.6	0.990	0.656	0.003	0.366	0.001	2.02	0.36
PT21C1	74.85	15.70	0.39	8.28	0.015	–	99.2	0.984	0.674	0.009	0.351	0.001	2.02	0.34
PT21D1	74.75	15.02	0.28	8.83	0.014	–	98.9	0.986	0.648	0.006	0.376	0.001	2.02	0.37
PT21E1	76.74	14.47	0.22	8.97	0.022	–	100.4	0.998	0.615	0.005	0.376	0.001	2.00	0.38
PT21F1	75.19	14.60	0.26	9.02	0.026	–	99.1	0.991	0.629	0.006	0.383	0.001	2.01	0.38
PT21F2	75.96	15.11	0.32	8.33	0.000	–	99.7	0.994	0.647	0.007	0.352	0.000	2.00	0.35
PT21F3	75.91	14.36	0.19	9.08	0.001	–	99.5	0.996	0.616	0.004	0.384	0.000	2.00	0.38
PT21F4	75.54	14.85	0.46	8.55	0.027	–	99.4	0.991	0.637	0.010	0.362	0.001	2.00	0.36
PT11A1	75.57	17.73	0.31	6.08	0.030	–	99.7	0.989	0.758	0.007	0.257	0.002	2.01	0.25
PT11B1	75.91	17.65	0.69	6.09	0.015	0.045	100.4	0.985	0.749	0.016	0.255	0.001	2.01	0.25
PT11B2	75.45	18.04	0.12	6.11	0.024	0.272	100.0	0.987	0.772	0.003	0.258	0.001	2.02	0.25
PT11C1	75.09	16.39	0.30	7.41	0.018	–	99.2	0.988	0.705	0.007	0.314	0.001	2.01	0.31
PT11C2	74.86	16.81	0.22	6.70	0.029	0.072	98.7	0.991	0.727	0.005	0.286	0.002	2.01	0.28
PT11D1	76.10	17.53	0.53	5.98	0.048	–	100.2	0.990	0.746	0.012	0.251	0.003	2.00	0.25
PT11D2	76.32	17.69	0.42	5.74	0.018	–	100.2	0.994	0.753	0.010	0.241	0.001	2.00	0.24
PT11E1	73.52	18.27	0.66	5.90	0.014	–	98.4	0.973	0.790	0.015	0.252	0.001	2.03	0.24
PT11E2	74.95	17.75	0.41	5.99	0.008	–	99.1	0.986	0.763	0.009	0.254	0.000	2.01	0.25
PT11F1	73.64	17.72	0.70	6.12	0.027	–	98.2	0.976	0.768	0.016	0.262	0.001	2.02	0.25
PT11F2	74.97	17.74	0.18	5.78	0.013	–	98.7	0.992	0.767	0.004	0.247	0.001	2.01	0.24

(Fig. 9b). Irber (1999) has quantified the degree of tetrad effect (TE_{1-3}) by determining the deviation of the first and third tetrad of granite REE patterns from a hypothetical tetrad effect-free REE pattern. The large majority of wolframite are characterized by significant tetrad effect ($TE_{1-3} > 1.1$) (Table 3). Element pairs Zr/Hf and Y/Ho of wolframite are remarkably fractionated and these ratios ($Zr/Hf = 13.4\text{--}34.6$, $Y/Ho = 10.0\text{--}14.4$) fall outside of CHARAC (CHArge-and-Radius-Controlled) field defined by Bau (1996) (Fig. 10).

4.5. Hydrogen and oxygen stable isotopes

The H isotopic compositions of the fluids hosted by quartz and wolframite were directly obtained through the analyses by mass spectrometer. The δD values of fluid hosted by quartz lie in a narrow range between -65.6 and $-70.5\text{\textperthousand}$ (Table 4). The δD values of fluid trapped in wolframite samples and cassiterite samples vary from -67.6 to $-78.9\text{\textperthousand}$ and -72.3 to $-78.3\text{\textperthousand}$, respectively (Table 4).

Twenty O isotope analyses were performed on carefully handpicked mineral separates of quartz, wolframite and cassiterite of 11 samples from main mineralized stage. The $\delta^{18}\text{O}$ values for the individual minerals are all positive and have relatively narrow ranges of $10.3\text{--}13.7\text{\textperthousand}$ for quartz, $2.5\text{--}6.8\text{\textperthousand}$ for wolframite and $6.1\text{--}7.2\text{\textperthousand}$ for cassiterite (Table 4). Calculated O isotopic equilibrium temperature between quartz and wolframite are in the range of $371\text{--}579^\circ\text{C}$, about 100°C higher than the fluid inclusion homogenization temperatures. Thus, we adopted the highest fluid inclusion homogenization temperature about 360°C for calculating O isotopic compositions of ore fluids. The results show that the $\delta^{18}\text{O}$ values of ore fluids equilibrated with quartz, wolframite and cassiterite are from 5.3 to $8.6\text{\textperthousand}$, 5.0 to $9.3\text{\textperthousand}$, and 9.5 to $10.6\text{\textperthousand}$, respectively (Table 4).

5. Discussion

5.1. Sources of ore-forming fluids

The source and nature of ore-forming fluids of Piaotang wolframite-quartz vein tungsten deposit in the Nanling W-Sn metallogenic province have been studied (Wang et al., 2009; Ni et al., 2015; Legros et al., 2018a). Fluid inclusions trapped in ore and gangue minerals from the vein systems are dominantly liquid-vapor two phase inclusions. Microthermometry data indicate homogenization temperature (T_h) and salinity range from 170 to 369°C and 4.3 to 9.0 wt\% eq. NaCl , respectively (Ni et al., 2015). Stable isotope analyses (H-O) of the FIs hosted by quartz and wolframite from this deposit have been performed. $\delta^{18}\text{O}$ values of quartz and wolframite are $11.6\text{\textperthousand}$ and $-3.0\text{\textperthousand}$, respectively (Legros et al., 2018b). Quartz and wolframite hosted FIs have δD values of -54 to $-51\text{\textperthousand}$ and -77 to $-76\text{\textperthousand}$, respectively (Legros et al., 2018b). Helium (He) and argon (Ar) isotopic compositions of FIs entrapped in wolframite and sulphide minerals from the Piaotang vein-type tungsten deposits also have been carried out. $^3\text{He}/^4\text{He}$ ratios vary from 0.17 to 0.86 R/R_A and $^{40}\text{Ar}/^{36}\text{Ar}$ ratios from 355 to 591 (Wang et al., 2009). The compositions and conditions of FIs from this vein-type tungsten deposits are interpreted as either mixing between magmatic and meteoric water or single magmatic fluid. The origin of ore-forming fluids remains contentious.

We have calculated the oxygen and hydrogen isotope composition of the ore-forming fluids focusing on the main mineralization stage (stage I) to constrain the most likely fluid source for the Piaotang tungsten deposit. The isotopic composition of the early fluids, which were equilibrium with stage I wolframite, cassiterite and quartz, is very close to magmatic water values (Fig. 11). The different fluid inclusion types show a strong similarity in chemical compositions, showing Rb/

Table 3

Trace elements of representative wolframite from the Piaotang tungsten deposit.

Spot	PT8A1	PT8B1	PT8C1	PT8D2	PT8E1	PT8E2	PT8F1	PT8F2	PT8F3	PT11A1	PT11B1	PT11B2	PT11C1	PT11C2	PT11D1	PT11D2	PT11E1
Li	0.88	0.60	0.25	0.62	0.85	0.18	0.41	0.79	1.14	0.02	0.31	0.00	0.32	0.00	1.15	0.79	0.17
Sc	202.05	64.50	52.04	82.37	36.89	123.67	48.79	101.64	106.18	6.58	7.20	7.60	13.09	8.63	9.00	11.47	11.71
Ti	79.66	18.17	19.34	38.44	19.62	55.93	22.91	66.88	17.22	6.48	8.65	9.66	3.46	5.94	5.41	16.81	16.94
V	0.83	0.50	0.31	0.42	0.34	1.41	0.39	0.88	0.68	0.23	0.02	0.00	0.04	0.00	0.00	0.14	0.01
Cr	0.57	2.28	0.91	9.96	0.00	0.35	2.19	0.00	2.27	0.60	0.19	0.09	0.00	0.72	0.33	0.00	0.00
Co	0.29	0.79	0.62	0.75	0.62	1.01	1.16	1.20	1.21	0.62	0.56	0.41	0.58	0.67	0.65	1.21	0.45
Ni	0.03	0.48	0.31	0.24	0.19	0.00	0.91	0.09	0.19	0.00	0.11	0.00	0.05	0.35	8.84	0.26	0.00
Cu	2.16	0.12	2.73	0.40	0.05	0.00	4.72	0.15	0.03	1.11	0.21	0.04	0.08	0.78	0.05	0.00	0.09
Zn	26.2	189.2	163.6	155.8	202.9	117.8	193.4	94.8	101.3	166.0	168.3	188.5	191.5	188.5	181.3	185.0	144.0
Ga	0.04	0.04	0.15	0.02	0.07	0.03	0.13	0.08	0.02	0.01	0.05	0.33	0.03	0.00	0.05	0.09	0.05
Rb	0.04	0.00	0.06	0.02	0.00	0.01	0.04	0.03	0.06	0.06	0.03	0.56	0.03	2.14	0.12	0.04	0.01
Sr	0.07	0.04	0.87	0.36	0.06	0.04	0.50	0.13	0.07	0.02	0.02	0.01	0.02	0.03	0.02	0.03	0.00
Y	35.40	49.87	74.86	76.70	39.57	68.99	58.96	58.10	58.20	22.57	25.42	29.54	31.89	28.05	29.29	40.79	46.05
Zr	57.73	35.68	43.90	51.70	33.23	53.19	60.21	25.02	20.84	9.51	21.55	30.23	10.66	8.58	16.92	33.14	30.23
Nb	5550	2815	3523	4021	3042	4158	3765	3091	2614	1635	2430	2830	1452	2048	2320	3774	2741
Mo	2.64	5.62	4.70	4.11	4.67	5.14	5.66	5.53	3.99	4.68	3.73	3.94	5.79	6.32	4.25	4.64	3.38
Cd	0.22	0.41	0.92	1.54	0.76	0.48	0.47	0.20	0.20	0.94	0.58	0.77	0.29	0.63	0.79	0.71	0.81
In	17.03	21.46	16.04	19.68	21.23	15.75	31.49	14.50	21.97	9.39	5.84	11.13	15.01	11.98	13.65	17.28	4.86
Sn	258.3	102.9	154.5	215.2	134.7	134.2	211.2	52.5	101.4	33.8	50.9	75.5	35.7	31.1	66.5	142.1	128.2
La	0.02	0.01	0.02	0.02	0.01	0.00	0.01	0.03	0.01	0.03	0.00	0.04	0.01	0.00	0.00	0.01	0.01
Ce	0.10	0.03	0.05	0.11	0.01	0.04	0.05	0.03	0.03	0.06	0.03	0.09	0.01	0.02	0.03	0.07	0.04
Pr	0.02	0.01	0.02	0.03	0.02	0.04	0.02	0.03	0.00	0.01	0.01	0.06	0.01	0.00	0.01	0.00	0.01
Nd	0.27	0.14	0.23	0.43	0.20	0.32	0.15	0.30	0.18	0.10	0.11	0.11	0.14	0.10	0.15	0.14	0.17
Sm	0.78	0.72	1.35	1.52	0.87	1.25	1.11	1.56	1.08	0.47	0.51	0.71	0.73	0.64	0.63	0.80	0.96
Eu	0.13	0.06	0.17	0.21	0.10	0.07	0.13	0.05	0.03	0.04	0.06	0.06	0.07	0.09	0.04	0.12	0.10
Gd	1.91	3.24	5.09	5.39	2.53	4.66	3.73	4.62	3.61	1.50	1.78	2.25	2.51	1.99	1.90	2.83	3.16
Tb	1.08	1.51	2.38	2.37	1.10	2.12	1.78	2.01	1.77	0.70	0.78	0.81	1.00	0.89	0.85	1.18	1.21
Dy	12.12	15.33	24.09	24.69	12.93	20.96	18.44	18.08	18.76	7.06	8.10	9.02	10.78	9.55	8.71	11.79	12.98
Ho	3.55	3.97	6.62	6.40	3.51	5.19	5.29	4.28	4.78	1.80	1.96	2.41	2.84	2.48	2.23	3.19	3.47
Er	17.36	18.14	28.12	28.22	16.99	21.27	22.90	17.62	20.30	7.84	8.75	10.72	12.55	10.97	9.94	13.49	15.29
Tm	4.78	4.85	6.97	6.86	4.64	5.36	6.19	4.25	5.10	1.95	2.34	2.81	3.28	2.72	2.59	3.46	3.72
Yb	57.18	52.98	74.80	74.86	55.59	56.70	69.90	42.99	55.39	23.19	24.59	29.71	35.55	30.85	29.48	40.47	43.66
Lu	10.48	9.75	13.47	12.96	10.52	9.70	12.97	7.18	9.75	4.54	4.72	5.59	6.78	5.69	5.52	7.39	7.95
Hf	3.36	1.99	1.46	2.09	1.39	3.97	2.44	1.58	1.03	0.57	1.22	1.74	0.52	0.31	0.70	1.31	1.22
Ta	228	179	228	290	215	318	228	83	311	128	190	230	49	94	183	555	412
Bi	0.08	0.04	0.07	0.01	0.06	0.04	0.00	0.05	0.05	0.11	0.07	0.07	0.05	0.05	0.06	0.07	0.05
Pb	0.78	0.14	1.24	1.07	0.10	0.33	1.26	0.19	0.35	0.40	0.12	0.12	0.18	0.14	0.13	0.23	0.12
Th	0.86	0.20	0.40	0.88	0.29	0.27	0.41	0.50	0.16	0.26	0.11	0.13	0.12	0.09	0.23	0.47	0.47
U	24.4	12.8	25.9	29.3	19.1	15.0	33.6	8.0	8.8	6.0	8.5	11.5	6.3	5.8	12.2	30.8	34.6
Zr/Hf	17.2	17.9	30.1	24.7	24.0	13.4	24.7	15.8	20.2	16.6	17.7	17.4	20.4	27.2	24.2	25.3	24.8
Y/Ho	10.0	12.6	11.3	12.0	11.3	13.3	11.1	13.6	12.2	12.6	13.0	12.3	11.2	11.3	13.1	12.8	13.3
TE ₁₋₃	1.1	1.0	0.9	1.2	0.6	2.5	1.7	0.7	0.6	1.1	1.6	1.9	0.7	0.5	2.3	0.4	1.1
8Eu	0.3	0.1	0.2	0.2	0.1	0.2	0.1	0.0	0.1	0.2	0.1	0.2	0.3	0.1	0.2	0.2	0.2

PT11E2	PT11F1	PT11F2	PT21A1	PT21B1	PT21B2	PT21C1	PT21D1	PT21E1	PT21F1	PT21F2	PT21F3	PT21F4
0.00	0.90	0.37	0.24	0.00	0.17	0.35	0.20	–	0.00	0.00	0.03	0.32
10.82	16.20	8.21	6.71	12.59	10.70	13.17	10.86	11.25	12.95	10.94	11.46	9.55
19.29	41.43	12.79	4.88	5.23	4.59	4.32	5.48	8.37	8.12	7.51	8.91	7.90
0.03	0.19	0.00	0.09	0.05	0.03	0.10	0.05	0.00	0.05	0.07	0.04	0.06
0.62	0.00	0.75	41.87	0.59	6.66	0.43	5.60	0.16	0.69	0.05	3.24	0.00
0.55	0.29	0.54	1.23	1.07	1.16	1.00	0.85	1.06	0.97	1.13	1.16	1.25
0.07	0.17	0.00	0.00	0.14	0.00	0.23	0.00	0.00	0.04	0.24	0.33	0.18
0.08	0.07	0.07	0.26	0.02	0.57	0.09	0.12	0.00	0.16	0.04	0.00	0.00
175.3	96.6	137.2	200.9	205.8	207.3	207.0	177.2	186.4	182.1	175.9	182.4	176.6
0.00	0.02	0.03	0.06	0.06	0.00	0.03	0.01	0.02	0.03	0.00	0.02	0.02
0.02	0.07	0.06	0.00	0.02	0.00	0.03	0.03	0.02	0.02	0.00	0.04	1.80
0.14	0.02	0.03	0.09	0.04	0.07	0.09	0.05	0.05	0.06	0.04	0.12	0.09
43.18	49.20	30.51	23.78	37.38	31.38	44.31	36.71	26.68	36.27	32.17	33.66	28.79
44.86	41.14	19.78	4.87	16.93	10.82	14.80	11.62	46.13	32.10	23.64	42.69	16.15
4320	3666	3016	1573	2072	1793	2087	1834	1683	2448	2020	2481	1427
3.67	2.55	3.17	10.70	9.75	9.61	10.37	9.29	11.80	9.66	10.73	10.44	10.51
0.73	0.37	0.53	0.27	0.24	0.39	0.75	0.45	0.45	0.43	0.15	0.29	0.40
21.85	1.97	1.43	13.30	17.06	15.33	23.36	18.43	16.46	17.26	15.63	15.23	15.23
171.6	231.6	88.1	12.5	47.8	34.3	40.1	29.5	30.3	66.1	44.2	57.9	26.4
0.02	0.00	0.01	0.19	0.00	0.14	0.01	0.01	0.00	0.00	0.01	0.01	0.02
0.05	0.03	0.02	0.02	0.02	0.02	0.04	0.64	0.01	0.02	0.01	0.00	0.00
0.01	0.01	0.01	0.01	0.01	0.01	0.16	0.00	0.01	0.00	0.01	0.01	0.00
0.16	0.30	0.13	0.04	0.14	0.12	0.17	0.10	0.12	0.06	0.12	0.13	0.00
1.09	1.06	0.69	0.52	0.73	0.58	0.83	0.76	0.44	0.76	0.75	0.76	0.56
0.09	0.08	0.14	0.04	0.06	0.05	0.07	0.05	0.03	0.04			

Table 3 (continued)

PT11E2	PT11F1	PT11F2	PT21A1	PT21B1	PT21B2	PT21C1	PT21D1	PT21E1	PT21F1	PT21F2	PT21F3	PT21F4
13.95	13.02	8.12	8.06	10.47	9.16	14.54	12.03	8.45	10.52	9.65	9.83	8.45
3.62	3.42	2.12	2.35	2.91	2.56	4.26	3.62	2.16	3.06	2.61	2.81	2.44
16.26	15.42	8.92	10.41	14.40	12.60	20.38	17.28	10.28	14.76	12.29	12.63	11.48
4.20	4.15	2.37	2.68	3.63	3.28	5.25	4.59	2.80	3.91	3.23	3.42	3.06
47.12	51.42	27.21	30.83	44.73	38.71	62.06	53.78	33.75	46.32	39.29	40.59	35.94
8.71	10.13	5.07	5.37	8.27	6.98	11.54	9.58	6.17	8.41	7.31	7.40	6.75
1.87	2.20	0.89	0.16	0.71	0.46	0.43	0.47	3.20	1.94	1.53	2.98	0.98
699	597	272	54	220	136	150	107	37	105	44	82	14
0.04	0.05	0.07	0.04	0.04	0.04	0.07	0.03	0.04	0.46	0.01	0.03	0.05
0.19	0.28	0.31	0.13	0.18	0.10	0.06	0.09	0.11	0.17	0.14	0.22	0.09
0.57	0.61	0.43	0.06	0.11	0.10	0.12	0.05	0.04	0.09	0.07	0.14	0.07
46.7	36.0	19.9	2.6	5.4	3.8	7.4	6.1	3.1	7.4	4.9	5.9	4.2
24.0	18.7	22.2	29.6	23.7	23.3	34.6	24.8	14.4	16.6	15.4	14.3	16.5
11.9	14.4	14.4	10.1	12.9	12.2	10.4	10.2	12.4	11.8	12.3	12.0	11.8
0.9	1.1	–	1.6	0.1	1.7	0.2	4.4	–	1.9	0.8	0.5	–
0.2	0.1	0.4	0.1	0.2	0.2	0.1	0.1	0.1	0.1	0.2	0.2	0.1

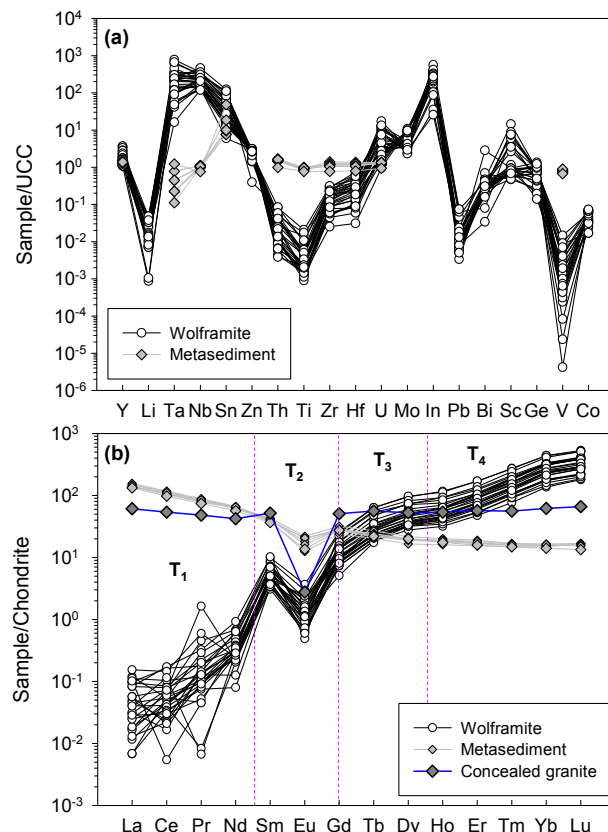


Fig. 9. Upper continent crust normalized multi-elements spider diagram (a) and Chondrite normalized REE patterns for wolframite from the Piaotang deposit.

Na ratios vary with Cs/Na ratio and Cs contents is positively correlated with As, W and Ti contents (Fig. 8). These correlation trends are interpreted as a single magmatic fluid source (Korges et al., 2018). Moreover, the trace element pattern of wolframite is remarkably different from those of hosting metasedimentary rocks (Fig. 9). Therefore, these isotopic signatures, coupled with correlation among elements in fluid inclusion, suggesting that without any fluid mixing at this time took place during wolframite precipitation. Thus, the ore-forming fluids was dominantly magmatic in origin. Metamorphic and meteoric fluids are not involved in the main mineralized stage although the quartz-wolframite veins were hosted by metasedimentary rocks.

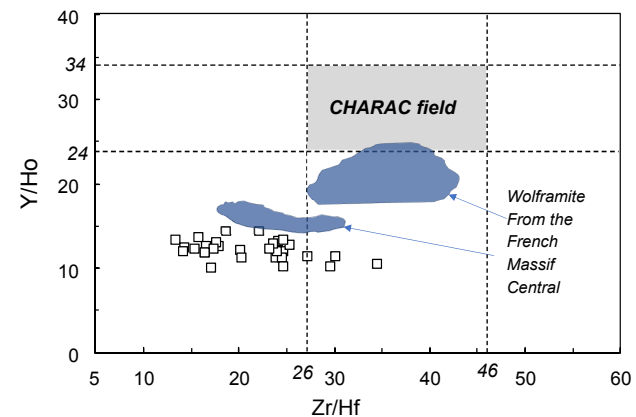


Fig. 10. Zr/Hf versus Y/Ho ratios in wolframite from the Piaotang tungsten deposit. The CHArge-and-Radiums-Controlled (CHARAC) field has been defined for common igneous rocks with $26 < \text{Zr/Hf} < 46$ and $24 < \text{Y/Ho} < 34$ (Bau, 1996). The data source of wolframite in the French Massif Central from Harlaux et al. (2018).

Table 4

Stable isotopes (H and O) for minerals and fluid from the Piaotang tungsten deposit.

Samples	Minerals	$\delta D_{\text{V-SMOW}} (\text{\textperthousand})$	$\delta^{18}\text{O}_{\text{V-SMOW}} (\text{\textperthousand})$	$\delta^{18}\text{O}_{\text{V-SMOW}} (\text{\textperthousand})$
		Fluid measured	Mineral measured	Fluid calculated
PT-5	Quartz	-68.2	10.3	5.3
PT-4	Quartz	-66.2	10.4	5.4
PT-6	Quartz	-70.5	11.1	6.1
PT-7	Quartz	-72.1	10.4	5.4
PT-8	Quartz	-67.8	11.6	6.6
PT-10	Quartz	-66.8	12.5	7.5
PT-11	Quartz	-69.3	13.6	8.6
PT-21	Quartz	-66.6	11.9	6.9
PT-22	Quartz	-66.1	10.5	5.5
PT-27	Quartz	-66.9	13.7	8.7
PT-28	Quartz	-65.5	13.1	8.1
PT-4	Wolframite	-67.6	5.5	8.0
PT-6	Wolframite	-78.9	4.9	7.4
PT-7	Wolframite	-74.0	2.5	5.0
PT-8	Wolframite	-67.8	4.1	6.6
PT-10	Wolframite	-71.2	6.8	9.3
PT-11	Wolframite	-76.9	6.6	9.1
PT-5	Cassiterite	-72.3	6.2	9.6
PT-7	Cassiterite	-75.8	6.1	9.5
PT-22	Cassiterite	-78.3	7.2	10.6

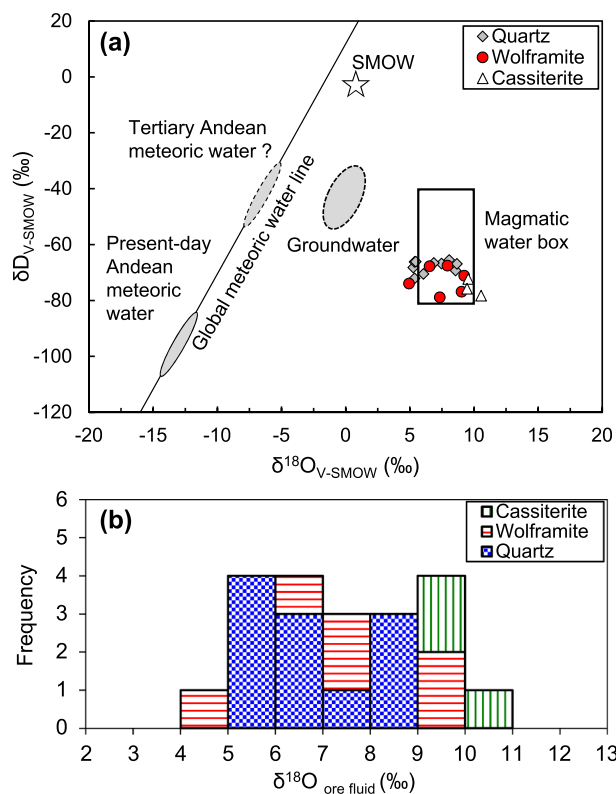


Fig. 11. Plot of δD versus $\delta^{18}\text{O}$ for ore-forming fluid from the Piaotang deposit (a), and distribution of the calculated $\delta^{18}\text{O}$ values for fluid in equilibrium with quartz, wolframite and cassiterite (b). The H-O isotopic compositions of magmatic water are from Sheppard (1994).

5.2. Magmatic fluid geochemistry and redox state

5.2.1. Magmatic fluid geochemistry

Element pairs Zr-Hf and Y-Ho, have the same charge and similar ionic radius, consequently should not fractionation (Dostal and Chatterjee, 2000). The Zr/Hf and Y/Ho ratios are expected to remain in the same value ranges. However, almost all the analyses of wolframite from the Piaotang deposit all fall outside the CHARAC field (Fig. 10), indicating that the ionic radius and the charge valence were not the only parameters controlling the mobility of the isovalent trace elements into the fluids precipitating the wolframites. Bau (1996) proposed that the non-CHARAC behavior of isovalent trace elements were controlled by ligands F and Cl complexation and transport in aqueous solution.

Moreover, the wolframite crystals precipitated in hydrothermal fluid show unusual tetrad effect REE patterns (Fig. 9b). Although the existence of the tetrad effect is still controversial, most of authors have argued that such REE patterns actually reflect a selective complexation of REE by efficient ligands F and Cl in hydrothermal fluid (Bau, 1996; Irber, 1999).

Therefore, the concentration of elements incorporated during the crystallization of wolframite reflects the specific chemical compositions of the hydrothermal fluid that contains high ligands F and Cl concentration. Generally, the volatile elements (F and Cl) and incompatible elements are enriched in highly evolved peraluminous granite and have high fluid-melt partition coefficient (mostly between 1 and 20) (Zajacz et al., 2008). LA-ICP-MS analyses show that the bulk incompatible elements Rb, Cs and Li are presented in FIs (Fig. 7), which coincide with the magmatic fluid exsolution likely from granite that concealed in the vicinity of the deposit.

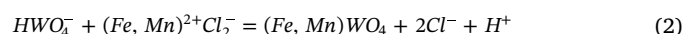
5.2.2. Redox state of magmatic fluid

The wolframite from the Piaotang tungsten deposit show obviously Eu negative anomaly (Fig. 9b) with δEu values of 0.1–0.4 (Table 3). Eu is a redox sensitive element and presents as Eu^{2+} and Eu^{3+} in different redox state. Compared with Eu^{2+} (1.17 Å), the ionic radius of Eu^{3+} is much closer to those of Fe^{2+} (0.78 Å) and Mn^{2+} (0.83 Å) (Shannon, 1976). Thus, Eu^{3+} is vastly more compatible than Eu^{2+} in the wolframite, more-oxidized melts will yield higher Eu contents in the wolframite. However, the wolframite from the Piaotang tungsten deposit depleted in Eu contents and display negative Eu anomaly, which imply Eu mainly presented as Eu^{2+} in magmatic fluid and cannot easily incorporate in wolframite. Thus, the ore-forming fluids of the Piaotang tungsten deposit are reduced in nature. Previous studies suggest tungsten mineralization is typically associated with reduced granitic magmas of crustal origin (Lecumberri-Sánchez et al., 2017). It is possible that the reduced ore-forming fluid of Piaotang tungsten deposit inherited from the reduced granitic magmas.

In summary, the ore-forming fluids of the Piaotang tungsten deposit are of reducing in nature and exsolved from the concealed granite in the vicinity of the deposit. These fluids contain all elements necessary for the formation of wolframite and incompatible elements as well as ligands F and Cl.

5.3. Wolframite precipitation

Based on the experimental study, NaHWO_4 , NaWO_4^- , HWO_4^- and WO_4^{2-} are the dominant tungsten species for the mineralizing fluids at a moderately acidic pH (between 4 and 6) and close to the fayalite-quartz-magnetite (FMQ) buffer (Gibert et al., 1992; Wood and Samson, 2000). The wolframite precipitation from a fluid can express by following reactions adapted to the physicochemical conditions (Wood and Samson, 2000).



On the basis of these chemical reaction, Dewaele et al. (2016) and Lecumberri-Sánchez et al. (2017) concluded that fluid-rock interaction was the controlling factor in wolframite precipitation in general. The metasedimentary rocks acted as a source of Fe and Mn while magmatic fluids contributed W for the formation of wolframite. However, the ore-forming fluids in the Piaotang tungsten deposit contain all elements necessary for the formation of wolframite (Fig. 7). Moreover, the surrounding metasedimentary rocks near the wolframite-bearing quartz vein contain low Fe ($\text{FeO} < 5.0$ wt%) and Mn ($\text{MnO} < 0.2$ wt%) contents (supplementary Table 1). The metasedimentary rocks proximal to the veins are altered weakly and are not systematically depleted in Fe, Mn and fluid-mobile elements (Fig. 6).

Alternatively, some researchers proposed that various types fluid mixing resulted in wolframite precipitation (Wei et al., 2012b, 2019; Dewaele et al., 2016; Legros et al., 2018b). However, the ore-forming fluids in the main mineralized stage in this research have homogeneous H-O isotopic compositions and show single magmatic fluid affinity (Fig. 11).

Thus, fluid-rock interaction and fluid mixing are not factor for controlling wolframite precipitation. Decreasing temperature and pressure of magmatic fluids has been considered decisive mechanism for formation wolframite quartz vein-type deposits (Thorn, 1988; Gibert et al., 1992; Korges et al., 2018). Within Piaotang deposits, wolframite FIs usually display a continuum between a high-salinity, high-temperature end-member and low-salinity, low-temperature end-member (Legros et al., 2018b). These FIs trapped in wolframite service as direct evidence for wolframite precipitation due to decreasing

temperature and pressure of magmatic fluid during infilling along fracture.

6. Conclusions

- (1) The ore-forming fluids in the Piaotang vein-type deposit was dominantly magmatic in origin. Metamorphic and meteoric fluids are not involved in main mineralized stage although the wolframite-quartz veins were hosted by metasedimentary rocks.
- (2) The ore-forming fluids of the Piaotang tungsten deposit are of reduced in nature and exsolved from the highly evolved melt that formed the concealed granite in the vicinity of the deposit. These fluids contain all elements necessary for the formation of wolframite and incompatible elements as well as ligands F and Cl.
- (3) Decreasing temperature and pressure of magmatic fluids have been responsible for wolframite precipitation during hydrothermal fluid infilling along fractures, rather than fluid mixing and fluid-rock interaction.

Acknowledgments

This research was financially supported by National Key R&D Program of China (Nos. 2016YFC0600405 and 2018YFC0603505), the National Science Foundation of China (Grant Nos. 41673054 and 41872097) and “CAS Hundred Talents” Project to Jian-Feng Gao. We thank the geologists of the Piaotang Tungsten Corporation for their assistance during our field work, and Dr. Zhi-Hui Dai and Yan-Wen Tang for their help with the analyses and technical assistance. We are grateful to the Editor Prof. Franco Pirajno, Guest Editor Prof. Yang Xiaoyong and two anonymous reviewers for their comments that help to improve our manuscript.

Appendix A. Supplementary data

Supplementary data to this article can be found online at <https://doi.org/10.1016/j.oregeorev.2019.102939>.

References

- Allan, M.M., Yardley, B.W., Forbes, L.J., Shmulovich, K.I., Banks, D.A., Shepherd, T.J., 2005. Validation of LA-ICP-MS fluid inclusion analysis with synthetic fluid inclusions. *Am. Mineral.* 90, 1767–1775.
- Audföt, A., Grüther, D., Heinrich, C., 2000. Magmatic-hydrothermal evolution in a fractionating granite: a microchemical study of the Sn-WF-mineralized Mole Granite (Australia). *Geochim. Cosmochim. Acta* 64, 3373–3393.
- Bau, M., 1996. Controls on the fractionation of isovalent trace elements in magmatic and aqueous systems: evidence from Y/Ho, Zr/Hf, and lanthanide tetrad effect. *Contribut. Mineral. Petro.* 123, 323–333.
- Deweale, S., De Clercq, F., Hulsbosch, N., Piessens, K., Boyce, A., Burgess, R., Muchez, P., 2016. Genesis of the vein-type tungsten mineralization at Nyakabingo (Rwanda) in the Karagwe-Ankole belt. *Central Afr. Miner. Depos.* 51, 283–307.
- Dostal, J., Chatterjee, A.K., 2000. Contrasting behaviour of Nb/Ta and Zr/Hf ratios in a peraluminous granitic pluton (Nova Scotia, Canada). *Chem. Geol.* 163, 207–218.
- Gibert, F., Moine, B., Schott, J., Dandurand, J.-L., 1992. Modeling of the transport and deposition of tungsten in the scheelite-bearing calc-silicate gneisses of the Montagne Noire. France. *Contribut. Mineral. Petro.* 112, 371–384.
- Goldstein, R.H., Reynolds, T.J., 1994. Systematics of fluid inclusions in diagenetic minerals. *SEPM Short C* 31, 1–199.
- Guillong, M., Meier, D.L., Allan, M.M., Heinrich, C.A., Yardley, B.W., 2008. Appendix A6: SILLS: a MATLAB-based program for the reduction of laser ablation ICP-MS data of homogeneous materials and inclusions. *Mineral. Assoc. Canada Short Course* 40, 328–333.
- Harlaux, M., Mercadier, J., Marignac, C., Peiffert, C., Cloquet, C., Cuney, M., 2018. Tracing metal sources in peribatholithic hydrothermal W deposits based on the chemical composition of wolframite: the example of the Variscan French Massif Central. *Chem. Geol.* 479, 58–85.
- Hsieh, P.-S., Chen, C.-H., Yang, H.-J., Lee, C.-Y., 2008. Petrogenesis of the Nanling Mountains granites from South China: constraints from systematic apatite geochemistry and whole-rock geochemical and Sr-Nd isotope compositions. *J. Asian Earth Sci.* 33, 428–451.
- Hu, R.-Z., Chen, W.T., Xu, D.-R., Zhou, M.-F., 2017. Reviews and new metallogenic models of mineral deposits in South China: an introduction. *J. Asian Earth Sci.* 137, 1–8.
- Hu, R.Z., Bi, X.W., Jiang, G.H., Chen, H.W., Peng, J.T., Qi, Y.Q., Wu, L.Y., Wei, W.F., 2012. Mantle-derived noble gases in ore-forming fluids of the granite-related Yaogangxian tungsten deposit. *Southeastern China Miner. Depos.* 47, 623–632.
- Hu, R.Z., Zhou, M.F., 2012. Multiple Mesozoic mineralization events in South China—an introduction to the thematic issue. *Miner. Depos.* 47, 579–588.
- Hulsbosch, N., Boiron, M.-C., Dewaele, S., Muchez, P., 2016. Fluid fractionation of tungsten during granite-pegmatite differentiation and the metal source of peribatholithic W quartz veins: evidence from the Karagwe-Ankole Belt (Rwanda). *Geochim. Cosmochim. Acta* 175, 299–318.
- Irber, W., 1999. The lanthanide tetrad effect and its correlation with K/Rb, Eu/Eu*, Sr/Eu, Y/Ho, and Zr/Hf of evolving peraluminous granite suites. *Geochim. Cosmochim. Acta* 63, 489–508.
- Korges, M., Weis, P., Lüders, V., Laurent, O., 2018. Depressurization and boiling of a single magmatic fluid as a mechanism for tin-tungsten deposit formation. *Geology* 46, 75–78.
- Lan, T.-G., Hu, R.-Z., Bi, X.-W., Mao, G.-J., Wen, B.-J., Liu, L., Chen, Y.-H., 2018. Metasomatized asthenospheric mantle contributing to the generation of Cu-Mo deposits within an intracontinental setting: a case study of the ~128Ma Wangjiazhuan Cu-Mo deposit, eastern North China Craton. *J. Asian Earth Sci.* 160, 460–489.
- Lecumberri-Sánchez, P., Vieira, R., Heinrich, C.A., Pinto, F., Wälde, M., 2017. Fluid-rock interaction is decisive for the formation of tungsten deposits. *Geology* 45, 579–582.
- Legros, H., Marignac, C., Tabary, T., Mercadier, J., Richard, A., Cuney, M., Wang, R.-C., Charles, N., Lespinasse, M.-Y., 2018a. The ore-forming magmatic-hydrothermal system of the Piaotang W-Sn deposit (Jiangxi, China) as seen from Li-mica geochemistry. *Am. Mineral.* 103, 39–54.
- Legros, H., Richard, A., Tarantola, A., Kouzmanov, K., Mercadier, J., Vennemann, T., Marignac, C., Cuney, M., Wang, R.-C., Charles, N., Bailly, L., Lespinasse, M.-Y., 2018b. Multiple fluids involved in granite-related W-Sn deposits from the world-class Jiangxi province (China). *Chem. Geol.*
- Li, Y., Gao, S., Hu, Z., Gao, C., Zong, K., Wang, D., 2010. Continental and oceanic crust recycling-induced melt-peridotite interactions in the trans-north China orogen: U-Pb dating, Hf isotopes and trace elements in zircons from mantle xenoliths. *J. Petrol.* 51, 537–571.
- Mao, J.W., Cheng, Y.B., Chen, M.H., Pirajno, F., 2013. Major types and time-space distribution of Mesozoic ore deposits in South China and their geodynamic settings. *Miner. Depos.* 48, 267–294.
- Matsuhashi, Y., Goldsmith, J.R., Clayton, R.N., 1979. Oxygen isotopic fractionation in the system quartz-albite-anorthite-water. *Geochim. Cosmochim. Acta* 43, 1131–1140.
- Ni, P., Wang, X.-D., Wang, G.-G., Huang, J.-B., Pan, J.-Y., Wang, T.-G., 2015. An infrared microthermometric study of fluid inclusions in coexisting quartz and wolframite from Late Mesozoic tungsten deposits in the Gannan metallogenic belt. *S. China Ore Geol. Rev.* 65, 1062–1077.
- Qi, L., Hu, J., Gregoire, D.C., 2000. Determination of trace elements in granites by inductively coupled plasma mass spectrometry. *Talanta* 51, 507–513.
- Roedder, E., 1984. Fluid Inclusions: Reviews in Mineralogy, vol. 12, 644 p.
- Romer, R.L., Kroner, U., 2016. Phanerozoic tin and tungsten mineralization—Tectonic controls on the distribution of enriched protoliths and heat sources for crustal melting. *Gondwana Res.* 31, 60–95.
- Shannon, R.T., 1976. Revised effective ionic radii and systematic studies of interatomic distances in halides and chalcogenides. *Acta Crystallogr. Sect. A Crystal Phys. Diffraction. Gen. Crystallogr.* 32, 751–767.
- Sheppard, S.M.F., 1994. Stable isotope and fluid inclusion evidence for the origin and evolution of Hercynian mineralizing fluids. In: Seltmann, R., Kämpf, H., Möller, P. (Eds.), *Metallogeny of Collisional Orogens*. Czech Geological Survey, Prague, pp. 49–60.
- Shen, J., Liu, L., Wang, D., Chen, Z., Ying, L., Huang, F., Wang, J., Zeng, L., 2015. A preliminary review of metallogenic regularity of tungsten deposits in China. *Acta Geol. Sin. English Ed.* 89, 1359–1374.
- Thorn, P.G., 1988. Fluid inclusion and stable isotope studies at the Chicote tungsten deposit, Bolivia. *Econ. Geol.* 83, 62–68.
- Van Daele, J., Hulsbosch, N., Dewaele, S., Boiron, M.C., Piessens, K., Boyce, A., Muchez, P., 2018. Mixing of magmatic-hydrothermal and metamorphic fluids and the origin of peribatholithic Sn vein-type deposits in Rwanda. *Ore Geol. Rev.* 101, 481–501.
- Wang, X.-D., Ni, P., Jiang, S.-Y., Zhao, K.-D., Wang, D.-G., 2009. The source of ore fluid in Piaotang tungsten deposit: evidence from He and Ar isotopes (in Chinese). *Chin. Sci. Bull.* 3338–44.
- Wei, W.-F., Hu, R.-Z., Bi, X.-W., Jiang, G.-H., Yan, B., Yin, R.-S., Yang, J.-H., 2019. Mantle-derived and crustal He and Ar in the ore-forming fluids of the Xihuashan granite-associated tungsten ore deposit. *South China Ore Geol. Rev.* 105, 605–615.
- Wei, W.-F., Hu, R.-Z., Bi, X.-W., Peng, J.-T., Su, W.-C., Song, S.-Q., Shi, S.-H., 2012a. Infrared microthermometric and stable isotopic study of fluid inclusions in wolframite at the Xihuashan tungsten deposit, Jiangxi province. *China Miner. Depos.* 47, 1–17.
- Wei, W., Hu, R., Bi, X., Peng, J., Su, W., Song, S., Shi, S., 2012b. Infrared microthermometric and stable isotopic study of fluid inclusions in wolframite at the Xihuashan tungsten deposit, Jiangxi province. *China Miner. Depos.* 47, 589–605.
- White, J.S., 1981. Wolframite Group. In: Frye, K. (Ed.), *Mineralogy. Encyclopedia of Earth Science*. Springer, Boston, MA, pp. 520–521.
- Wilkinson, J.J., 1990. The role of metamorphic fluids in the development of the Cornubian Orefield: fluid inclusion evidence from south Cornwall. *Mineral. Mag.* 54, 219–230.
- Wood, S.A., Samson, I.M., 2000. The hydrothermal geochemistry of tungsten in granitoid environments: I. Relative solubilities of ferberite and scheelite as a function of T, P, pH, and mNaCl. *Econ. Geol.* 95, 143–182.
- Yan, D.-P., Zhou, M.-F., Song, H.-L., Wang, X.-W., Malpas, J., 2003. Origin and tectonic significance of a Mesozoic multi-layer over-thrust system within the Yangtze Block (South China). *Tectonophysics* 361, 239–254.

- Yang, J.-H., Liu, L., Liu, J., 2017. Current progress and prospect for genesis of extensive Mesozoic granitoid and granitoid-related multi-metal mineralization in southern China (in Chinese with English Abstract). *Acta Mineral. Sin.* 791–800.
- Yang, J.-H., Kang, L.-F., Peng, J.-T., Zhong, H., Gao, J.-F., Liu, L., 2018. In-situ elemental and isotopic compositions of apatite and zircon from the Shuikoushan and Xihuashan granitic plutons: implication for Jurassic granitoid-related Cu-Pb-Zn and W mineralization in the Nanling Range. *South China Ore Geol. Rev.* 93, 382–403.
- Yuan, S., Williams-Jones, A.E., Mao, J., Zhao, P., Yan, C., Zhang, D., 2018. The origin of the Zhangjialong tungsten deposit, south China: implications for W-Sn mineralization in large granite batholiths. *Econ. Geol.* 113, 1193–1208.
- Zajacz, Z., Halter, W.E., Pettke, T., Guillong, M., 2008. Determination of fluid/melt partition coefficients by LA-ICPMS analysis of co-existing fluid and silicate melt inclusions: controls on element partitioning. *Geochim. Cosmochim. Acta* 72, 2169–2197.
- Zhang, L.G., Liu, J., Chen, Z., Zhou, H., 1994. Experimental investigations of oxygen isotope fractionation in cassiterite and wolframite. *Econ. Geol.* 89, 150–157.
- Zhang, R., Lu, J., Lehmann, B., Li, C., Li, G., Zhang, L., Guo, J., Sun, W., 2017. Combined zircon and cassiterite U-Pb dating of the Piaotang granite-related tungsten-tin deposit, southern Jiangxi tungsten district. *China Ore Geol. Rev.* 82, 268–284.
- Zhao, K.D., Jiang, S.Y., 2004. Mineral chemistry of the Qitianling granitoid and the Furong tin ore deposit in Hunan province, south China: Implications for the genesis of granite and related tin mineralization. *EMPGX Symposium Abstract. Lithos* 73, S124.
- Zhao, W.W., Zhou, M.-F., Li, Y.H.M., Zhao, Z., Gao, J.-F., 2017. Genetic types, mineralization styles, and geodynamic settings of Mesozoic tungsten deposits in South China. *J. Asian Earth Sci.* 137, 109–140.